

1  
2  
3  
4  
5  
6  
7  
8  
9  
10  
11  
12  
13  
14  
15  
16  
17  
18  
19  
20  
21

**A Regime-Dependent Retrieval Algorithm for  
Near-Surface Air Temperature and Specific Humidity from Multi-Microwave Sensors**

Lisan Yu\* and Xiangze Jin  
Woods Hole Oceanographic Institution, Woods Hole, MA

Remote Sensing of Environment  
May 2018

---

\* Corresponding author address: Dr. Lisan Yu, Department of Physical Oceanography, Mail Stop #21, Woods Hole Oceanographic Institution, Woods Hole, MA 02543. Email: lyu@whoi.edu

24

25 **Key words:**

26 Near-surface air temperature and specific humidity, moored surface buoys, retrieval algorithm,

27 microwave passive sensors, multisensor retrieval.

## Abstract

28  
29  
30 Near-surface specific humidity ( $q_a$ ) and air temperature ( $T_a$ ) over the global ocean are important  
31 meteorological variables, but they cannot be retrieved directly from remote sensing. Many efforts  
32 have been made to develop algorithms that derive  $q_a$  and  $T_a$  from multisensor microwave and/or  
33 infrared observations using in situ measurements as training datasets. However, uncertainty  
34 remains large in the resultant  $q_a$  and  $T_a$  retrievals. In this study, 147 moored surface buoys are  
35 used to examine how buoy measured  $q_a$  and  $T_a$  are related to satellite microwave brightness  
36 temperature (Tb) on the spatial scale from the warm/humid tropics to the cold/dry high latitudes.  
37 It is found that the Tb –  $q_a$  and Tb –  $T_a$  relations are structured along two distinct, near-linear  
38 bands, with the primary band in the warm/humid regime and a secondary (weaker) band in the  
39 cold/dry regime. The step-like transition (or separation) between the two regimes occurs at 8 –  
40 10 g kg<sup>-1</sup> for  $q_a$  and 14 – 17°C for  $T_a$ . The evidence suggests that one algorithm may not be  
41 sufficient to extract  $q_a$  and  $T_a$  from Tb in all regimes. Therefore, a high-latitude enhancement is  
42 added to the global algorithm so that the  $q_a$  and  $T_a$  retrievals in the dry/cold regime can be  
43 specifically addressed. The new algorithms are applied to 11 microwave sensors, including  
44 SSM/I, SSMIS, and AMSU-A, from 1988 to 2016. Based on the 475,717 buoy collocations  
45 during the 29-year period, the retrieved  $q_a$  and  $T_a$  have root-mean-square differences of 0.82 g  
46 kg<sup>-1</sup> and 0.51°C, respectively.

47

48

49

50

## 51 **1. Introduction**

52           Near-surface air temperature ( $T_a$ ) and specific humidity ( $q_a$ ) over the global ocean are  
53 important meteorological variables. They set one of the driving conditions for turbulent  
54 exchanges of heat and water vapor at the air-sea interface (Stephens 1990; Yu and Weller 2007;  
55 Lorenz et al. 2010), and influence many ocean and atmospheric processes that are central to the  
56 Earth's weather and climate (Bretherton et al. 2004; Sherwood et al.2010). Water vapor is a  
57 nature greenhouse gas. With the rise of atmospheric temperature in response to the addition of  
58 anthropogenic gases, there are more evaporation of water vapor from the ocean (Yu 2007) and  
59 more absorption of water wavpor in the air (Held and Soden 2006) which further increase  
60 atmospheric temperature. This positive water vapor feedback is regarded as a key driver of the  
61 amplification of any warming caused by changes in atmospheric CO<sub>2</sub> (Manabe and Wetherald,  
62 1967; Hansen et al. 1984). Thus, there is a pressing need for well-calibrated, consistent, and  
63 continuous long-term data records for  $T_a$  and  $q_a$  to keep tracking variability and long-term  
64 change of the near-surface thermal conditions and to improve the quantification and modeling of  
65 the water vapor feedback.

66           Measurements of  $T_a$  and  $q_a$  are conventionally obtained at sea by moored buoys and ships  
67 of opportunity, but these observations are sparse in both space and time (e.g. Kent and Taylor  
68 1996; Dai 2006; Willett et al. 2008; Berry and Kent 2009). Space-borne sensors that provide  
69 continuous global coverage would be a desirable observing platform. However, retrieving  $T_a$  and  
70  $q_a$  at a level of a few meters above the surface proves difficult for the space-borne technology,  
71 because the measured radiation is emitted from relatively thick atmospheric layers rather than  
72 from single levels (Schulz et al. 1993). Making use of satellite measured total column of water  
73 vapor (or total precipitable water (PW)) to estimate  $q_a$  and  $T_a$  at the near surface has been

74 actively investigated ever since the pioneer work by Liu and Niiler (1984), Liu (1986; 1988), and  
75 Liu et al. (1991). The Liu studies showed that most of the spatial and temporal variability of  
76 water vapor is confined in the lower part of the atmospheric column. The decoupling of the  
77 atmospheric boundary layer from the higher atmosphere enables the vertical coherence of the  
78 humidity variability, leading to a high correlation between the surface-level  $q_a$  and the total PW  
79 observed by radiosondes. Liu (1988) indicated that PW measured by scanning multichannel  
80 microwave radiometer (SMMR) on Seasat is similar in form to the PW observed by radiosondes  
81 (Liu and Niiler 1984; Liu 1986), both of which can be used to estimate  $q_a$  on monthly timescales  
82 with a root-mean-square (rms) error of about  $0.4 \text{ g kg}^{-1}$  in the tropics and  $0.8 \text{ g kg}^{-1}$  over the  
83 global ocean. Hsu and Blanchard (1989) examined the PW– $q_a$  relation in the context of 13 field  
84 experiments over the oceans, and suggested that the relation should also work for instantaneous  
85 surface humidity retrievals. Subsequent algorithm developments have been particularly boosted  
86 by the availability of a series of Special Sensor Microwave/Imager (SSM/I) onboard the Defense  
87 Meteorological Satellite Program (DMSP) satellites since July 1987, and by the launch of the  
88 Advanced Microwave Sounding Unit-A (AMSU-A) on the National Ocean and Atmospheric  
89 Administration (NOAA) series of polar orbiting meteorological satellites in May 1998. The  
90 SSM/I is a conically scanning microwave radiometer with seven frequency channels. The  
91 AMSU-A is a multi-channel microwave radiometer that performs atmospheric sounding of  
92 temperature and moisture levels by passively recording atmospheric microwave radiation in  
93 multiple wavelengths. A survey of the algorithms that have been developed in the past 30 years  
94 is provided in Table 1.

95         As shown in Table 1, the algorithm development can be loosely categorized into three  
96 stages. The first stage is represented by the work of Schulz et al. (1993) and Chou et al. (1995),

97 who used the SSM/I measurements to first determine the water vapor in the lowermost 500 m of  
98 the atmosphere and then predict  $q_a$ . This approach underscores the fact that for most oceanic  
99 situations, the water vapor in the homogenous atmospheric boundary layer can be related to  $q_a$  by  
100 a simple linear regression (Taylor 1982). The second stage is ushered in by Schlüssel et al.  
101 (1995), who proposed a direct  $q_a$  retrieval from SSM/I Tb in 5 channels (19v, 22v, 37v, 19h, and  
102 37h GHz, with h and v denote horizontal and vertical polarization, respectively). This approach  
103 seems to be able to reduce the error propagation associated with the two-step procedure of  
104 Schulz et al. (1993), leading to an improved  $q_a$  retrieval. The approach was subsequently  
105 extended to Tb measurements from other platforms including the Advanced Microwave  
106 Scanning Radiometer for EOS (AMSR-E), the WindSat Polarimetric Radiometer, and the  
107 Special Sensor Microwave Imager/Sounder (SSMIS) (Jones et al. 1999; Bentamy et al. 2003;  
108 Jackson et al. 2006; 2009; Kubota and Hihara 2008; Roberts et al. 2010). The third stage features  
109 the use of atmospheric soundings from instruments like the AMSU, the High-resolution Infrared  
110 Radiation Sounder (HIRS), and the Special Sensor Microwave Water Vapor Profiler (SSM/T and  
111 SSM/T-2). The sounders do not directly provide shallow surface measurements, but the detailed  
112 profile information observed by the sounders can help to remove the variability in the total  
113 column measurements that are not associated with the surface. Utilization of microwave and  
114 infrared sounders, with or without microwave radiometers, to estimate  $q_a$  and  $T_a$  has been  
115 explored by Shi (2001), Shi et al. (2012), Jackson et al. (2006; 2009), and Jackson and Wick  
116 (2010).

117         Ironically, despite the efforts and the progress that have been made,  $q_a$  and  $T_a$  remain the  
118 leading error source for satellite-based air–sea heat flux datasets (Curry et al. 2004; Jackson et al.  
119 2006; Prytherch et al. 2015). Jin et al. (2015) conducted a buoy-based evaluation of two satellite-

120 derived products: one is the  $q_a$  product by the Goddard Satellite-based Surface Turbulent Fluxes  
121 (GSSTF) v3 (Chou et al. 1995; Shie et al. 2012) and the other is the  $q_a$  and  $T_a$  products from the  
122 multi-instrument microwave regression (MIMR) by Jackson et al. (2006; 2009) and Jackson and  
123 Wick (2010). Evaluation with the 137 air-sea buoys over the global scale showed that the biases  
124 in  $q_a$  and  $T_a$  are strongly regime dependent, featuring warm and wet biases in the tropical  
125 warm/humid region and cold and dry biases in the extratropical cold/dry region. For instance, the  
126 mean difference between MIMR and buoy  $q_a$  changes from a wet bias of  $0.8 \text{ g kg}^{-1}$  in the tropical  
127 latitudes between  $10^\circ\text{S} - 10^\circ\text{N}$  to a dry bias of  $-0.8 \text{ g kg}^{-1}$  at high latitudes poleward of  $45^\circ$ . Jin et  
128 al. (2015) eventually obtained an improved analysis on  $0.25^\circ$  resolution through implementing a  
129 buoy-based bias correction to MIMR and GSSTF3 followed by an objective synthesis with the  
130  $1^\circ$ -gridded  $q_a$  analysis produced by the Objectively Analyzed air-sea Fluxes (OAFlux; Yu and  
131 Weller 2007; Yu et al. 2008). However, the extensive use of buoys and OAFlux- $1^\circ$  for bias  
132 correction at both regional and global scales is not a sustainable solution for improving the  $q_a$   
133 and  $T_a$  retrievals.

134 Esbensen et al. (1993) raised a cautious note about applying the Liu method to the global  
135 scale. When estimating  $q_a$  from SSM/I observations, they obtained systematic discrepancies of  
136 over  $2 \text{ g kg}^{-1}$  in the tropics. They postulated that in regions of persistent strong subsidence, most  
137 of the water vapor is trapped near the surface and so the Liu's method can work reasonably well.  
138 In regions of active convection, a significant amount of water vapor can exist aloft where it is  
139 acted upon by processes that are less correlated with humidity at the near-surface level. Hence,  
140 the Liu method in the tropics and the storm-tracked regions may not work in the same way as  
141 that in the middle and high latitudes. If this is the case, the regime-dependent biases in MIMR  
142 and GSSTF  $q_a$  (and  $T_a$ ) that are identified by Jin et al. (2015) may well be caused by error

143 compensations when fitting the regimes that have different vertical structures of water vapor.  
144 The retrieval algorithms for  $q_a$  and  $T_a$  that have been developed so far are based primarily on two  
145 approaches: linear regression (Schlüssel et al 1995; Bentamy et al. 2003; Jackson et al. 2006;  
146 2009; Kubota and Hihara 2008) and nonlinear artificial neural network (Jones et al. 1999; Shi  
147 2001; Shi et al. 2012; Roberts et al. 2010). All these algorithms require in situ observations as  
148 reference datasets to train the empirical relationships (or transfer functions) between the input  
149 ( $T_b$ ) and output ( $q_a, T_a$ ). Usually, the relationships are assumed globally valid and applicable to  
150  $q_a$  and  $T_a$  in all regimes. If the findings of Esbensen et al. (1993) hold true, a globally applicable  
151 algorithm would not be sufficient to represent the full range of the relations between  $T_b$  and ( $q_a,$   
152  $T_a$ ).

153           Moored air-sea buoys have been continually deployed in dynamically active regions  
154 since the late 1980s, providing high-frequency research-quality time series measurements over  
155 146 locations globally (Figure 1) (Send et al. 2010). They serve as anchor points for satellite  
156 retrievals (section 2). Therefore, the objective of this study is threefold: (i) to examine the  
157 relationships between satellite microwave  $T_b$  observations and buoy measurements of  $q_a$  and  $T_a$   
158 on the global scale (section 3), (ii) to explore an enhancement approach to address the challenges  
159 induced by regime differences (section 4), and (iii) to explore a synergistic strategy for  
160 multisensory retrieval of  $q_a$  and  $T_a$  starting from 1988 when SSM/I became available (also  
161 section 4). Evaluation with independent buoy measurements is conducted (section 5), and a  
162 summary and conclusion is given (section 6).

163

## 164 **2. Data**

### 165 2.1 Satellite sensors

166 This study uses Tb observations from microwave sensor series on the following satellite  
167 platforms: SSM/I sensors (F08, F10, F11, F13, F14, and F15) and SSMIS sensor (F17) on DMSP  
168 satellites, and AMSU-A sensors (N15, N16, N17, and N18) on NOAA meteorological satellites.  
169 The time line for each of the 11 sensors is shown in Figure 2, and general characteristics of the  
170 11 sensors are summarized in Table 2.

171 SSM/I was first launched in July 1987 on the DMSP satellite F08. The instrument has  
172 seven passive channels that sense vertically and horizontally polarized radiation at 19.3, 37.0,  
173 and 85.5 GHz and vertically polarized radiation at 22.2 GHz. It has a 1394 km scanning swath  
174 with a footprint ranging from 13 km to 69 km, depending on the channel and geographic location  
175 (Hollinger et al., 1990). SSMIS is a series of passive microwave conically scanning imagers and  
176 sounders onboard the DMSP satellites. It is designed to combine and extend the imaging and  
177 sounding capabilities of three previously separate DMSP microwave sensors: the SSM/T-1  
178 temperature sounder, the SSMI/T- 2 moisture sounder, and the SSM/I. The SSMIS instrument  
179 measures microwave energy at 24 channels, with 21 discrete frequencies from 19 to 183 GHz  
180 and a swath width of 1700 km. Although 4 SSMIS instruments have flown subsequently since  
181 October 2003, only F17 Tb observations were used. SSMIS F16 has radiance anomalies due to  
182 calibration issues ([www.rmess.com](http://www.rmess.com)), and F18 and F19 datasets were not available when the work  
183 commenced.

184 The AMSU-A is a cross-track scanner with 15 channels (Goldberg, 1999), with 11  
185 channels (4 through 14) located in the 50-60 GHz oxygen absorption band that is capable of  
186 sampling the temperature of the atmosphere in various layers. It has approximately 50 km spatial  
187 resolution at nadir and a swath width of 2343 km. The Tb observations from SSM/I and SSMIS

188 are version 7 products processed by Wentz (2013) and those from AMSU-A by Zou and Wang  
189 (2013).

190

## 191 2.2 Moored surface buoys

192 Of all 147 moored surface buoys assembled (Figure 1), 68 buoys are from the Tropical  
193 Atmosphere Ocean/TRIangle Trans-Ocean buoy Network (TAO/TRITON) in the tropical Pacific  
194 Ocean (McPhaden et al., 1998), 21 are from the Pilot Research Moored Array in the Atlantic  
195 (PIRATA) (Bourlès et al., 2008), and 28 are from the Research Moored Array for Africa-Asian-  
196 Australian Monsoon Analysis and Prediction (RAMA) in the tropical Indian Ocean (McPhaden  
197 et al., 2009). The remaining 30 buoys that are not associated with the tropical moored arrays are  
198 listed in Table 3. At each buoy location, measurements of air-sea variables (e.g. near-surface  
199 temperature, humidity, wind, barotropic pressure, downwelling short- and/or long-wave, sea-  
200 surface temperature (SST), etc.) are provided at every 10- to 15-min intervals.

201 Collocated satellite Tb retrievals and buoy measurements of  $q_a$  and  $T_a$  were compiled for  
202 2010 to allow examination of the relationships between these variables. The year 2010 was  
203 chosen because it was the time that the South Ocean Flux Station (SOFS) started to operate  
204 (Schulz et al. 2012) and the buoy provides a valuable reference for the southern high latitudes.  
205 There were 125 buoy time series available in 2010, with 117 from the three tropical moored  
206 arrays. The 8 other buoys include the surface mooring at the Kuroshio Extension Observatory  
207 (KEO) (Cronin et al., 2008), the Ocean Station PAPA (OSP) in the Gulf of Alaska (Kamphaus et  
208 al. 2008), the SOFS (Schulz et al. 2012), the Woods Hole Oceanographic Institution (WHOI)  
209 Hawaii Ocean Timeseries Site (WHOTS), the WHOI Northwest Tropical Atlantic Station  
210 (NTAS), the WHOI Stratus Deck regions of the eastern tropical Pacific (STRATUS), and 2

211 buoys from the National Data Buoy Center (NDBC) at Stations 46075 (160.817°W, 53.983°N)  
212 and 46085 (142.492°W, 55.868°N).

213         The development of the retrieval algorithms used 125 buoys in 2010. There are additional  
214 22 buoys that were deployed either before or after 2010, and these buoys plus the 125 buoys  
215 outside of 2010 were taken as independent validation data in the study.

216         The three tropical arrays carry the Automated Temperature Line Acquisition System  
217 (ATLAS) buoys or TRITON buoys (McPhaden et al., 1998). The WHOI buoys are equipped  
218 with the Improved METeorology (IMET) or Air Sea Interaction–METeorology (ASIMET)  
219 systems (Weller and Anderson, 1996; Moyer and Weller, 1997). A comparison of the ATLAS,  
220 TRITON, and IMET mooring meteorological sensors using a land-based cross-validation  
221 approach showed that the three systems measure to equivalent standards of accuracy (Payne et  
222 al., 2002). The relative humidity (RH) sensors are accurate to  $\pm 1\%$  RH and air temperature  
223 sensors are better than  $0.1^\circ\text{C}$  (Colbo and Weller, 2009).

224

### 225 **3. Global relationships between satellite $T_b$ and buoy measured $q_a$ and $T_a$**

226         The  $T_b$  observations from four vertically polarized channels were used to relate buoy  
227 measured  $q_a$  and  $T_a$ , with three frequencies (19, 22, and 37 GHz) from SSM/I and SSMIS, and  
228 one (52 GHz) from AMSU-A. The selection is in line with the findings of Jackson et al. (2006)  
229 that these channels are most sensitive to water vapor. Microwave spectroscopy has a weak water  
230 vapor absorption line centered on the 22 GHz (Liu 1988; Wentz 1997), which enables the signal  
231 from the water vapor to be better separated from the signal from the cloud (i.e., dew condensed  
232 water). The 19 and 37 GHz bands are away from the spectral peak and are more absorbent to  
233 water vapor. The AMSU 52 GHz channel is near the characteristic absorption peak of oxygen

234 and contains information about the physical temperature of the atmospheric molecules and its  
235 perspective profiles. A combination of the two spectra, water vapor and oxygen, can provide  
236 needed information of water vapor and temperature.

237 Buoy  $q_a$  and  $T_a$  are usually measured at a height of 2 – 3 m above the water (McPhaden  
238 et al., 1998; Colbo and Weller, 2009). These  $q_a$  and  $T_a$  measurements were height adjusted to the  
239 standard 2m using the Coupled Ocean-Atmosphere Response Experiment (COARE) version 3.5  
240 algorithm (Fairall et al. 2003). Accordingly, the reference height for the  $q_a$  and  $T_a$  retrievals is set  
241 at 2m in this study. This is different from most satellite retrieval algorithms that use ship-based  
242 measurements as reference and obtain  $q_a$  and  $T_a$  at a height of 10 m (Bentamy et al. 2003;  
243 Jackson et al. 2006; 2009; Kubota and Hihara 2008; Roberts et al. 2010; Shi et al. 2012). The 2  
244 m  $q_a$  and  $T_a$  have the advantage of making a direct comparison with the atmospheric reanalysis,  
245 as atmospheric models output the two variables at the 2-m height.

246 Collocated satellite Tb retrievals and buoy measurements of  $q_a$  and  $T_a$  were compiled for  
247 the year of 2010. Three sensors were in operation in 2010 (Figure 2), SSMIS F17, AMSU-A  
248 N15 and N18. To illustrate the spatial distribution of Tb variability, daily Tb fields from F17 19,  
249 22, 37, and N15 52 GHz are shown on January 1<sup>st</sup>, 2010 (Figure 3). These daily fields were  
250 constructed from ascending and descending passes associated with each channel. Our calculation  
251 shows that SSMIS provides 84% of daily coverage over the global ocean and AMSU-A provides  
252 97%. The spatial patterns of Tb from the three SSMIS channels all look similar, but the  
253 magnitude of Tb is largest at 22 GHz because the weak water vapor absorption line near the 22  
254 GHz is the best place for observing emission from the lower atmosphere. The AMSU measures  
255 the atmospheric temperature profiles at channels near 60 GHz, which is an oxygen absorption

256 line. The ASMU-A Tb at 52 GHz is known for its sensitivity to temperature near the surface (e.g.  
257 Jackson et al. 2006).

258 To collocate satellite Tb measurements with buoy  $q_a$  and  $T_a$  measurements, we used a  
259 time and space window of 90 mins and 50 km. The space-window of 50 km is selected on the  
260 basis of spatial resolution of the sensors. The spatial resolution is 50 km for AMSU, and 28 – 43  
261 km for SSM/I and SSMIS (Zou and Wang 2013; Wentz 2013). The collocation times were based  
262 on the local overpass time of the sensor. The DMSP polar-orbiting satellite F17 has local  
263 ascending overpass times at 6:25 pm. The NOAA polar-orbiting satellites fly Sun synchronous  
264 orbits, with local ascending overpass times of ~2 pm for N18 and ~7 pm for N15 in 2010. F17  
265 and N15 can be collocated within the time window of 90 mins, while the 2 pm N18 does not  
266 collocate with either of them. To ensure the coherence in observed variability between sensors,  
267 only F17 and N15 were taken as reference data. A total of 31,793 buoy-SSMIS collocations and  
268 36,291 buoy-AMSU-A collocations were obtained. The triple collocations between buoy, SSMIS,  
269 and AMSU-A totaled 17,975. Note that the search period for the satellite-buoy collocations were  
270 limited to the year of 2010 at all buoy sites except for SOFS. As the buoy at the latter site was  
271 deployed in March 2010, the search period was extended to February 2011 to make it a full year.

272 The scatter diagrams of the Tb– $q_a$  collocations (Figure 4) are used to examine how the  
273 two variables correlate on the global scale. Strikingly, two bands of the Tb– $q_a$  relation are  
274 displayed at all four frequencies, with a primary band in the humid regime (i.e., buoy  $q_a$  higher  
275 than  $10 \text{ g kg}^{-1}$ ) and a secondary (weaker) band in the dry regime (i.e. buoy  $q_a$  lower than  $8 \text{ g kg}^{-1}$ ).  
276 For each regime, the Tb– $q_a$  relation is near linear at 22 and 52 GHz channels, showing that Tb is  
277 most sensitive to the near-surface humidity at the spectral peaks of water vapor and oxygen. At  
278 19 and 37 GHz channels, the relation is near linear in the dry regime but highly nonlinear in the

279 highly humid regime. The increase of Tb with  $q_a$  hits a plateau when  $q_a$  reaches  $\sim 20 \text{ g kg}^{-1}$ , and  
280  $q_a$  remains little changed with further increase in Tb.

281 The step-like regime shift in the Tb- $q_a$  relation is equally featured in the scatter diagrams  
282 of the Tb- $T_a$  collocations (Figure 5), with one band in the warm regime (i.e. buoy  $T_a$  higher than  
283  $17^\circ\text{C}$ ) and the other in the cold regime (i.e. buoy  $T_a$  lower than  $14^\circ\text{C}$ ). The transition between the  
284 warm and cold regimes occurs for  $T_a$  in the range of  $14\text{--}17^\circ\text{C}$ , which is more distinct and step-  
285 like than the transition between the humid and dry regimes (Figure 4). In the cold regime, the  
286 relationship between the two variables is generally linear though the scatter is wider. On the  
287 other hand, the outstanding features that are identified in the Tb- $q_a$  scatter diagrams are also  
288 observed. For instance, the 22 and 52 GHz channels produce a more linear Tb- $T_a$  relation than  
289 the 19 and 37 GHz channels. The Tb- $T_a$  relation has a plateau when  $T_a$  exceeds  $26^\circ\text{C}$ , where  
290 further increase in Tb is not accompanied by an increase in  $T_a$ .

291 These patterns of the Tb- $q_a$  and Tb- $T_a$  relations (Figures 4-5) are in good agreement with  
292 the patterns derived from ship reports that were constructed by Jackson et al. (2006). However,  
293 the step-like shift in the Tb- $q_a$  and Tb- $T_a$  relations between the tropical warm/humid and the  
294 higher-latitude cold/dry zones are more vividly captured by buoy measurements in this study.  
295 The regime-dependent shift in the relation indicates that a global model is not sufficient to  
296 represent the characteristics of the relation in each regime.

297

## 298 **4. A global retrieval algorithm with high-latitude enhancement**

### 299 **4.1 The retrieval strategy**

300 In the literature (see Table 1), two general methods are used to develop the Tb-based  
301 retrieval algorithms: a multivariate linear regression (e.g., Schlüssel et al. 1995; Bentamy et al.

2003; Kubota and Hihara 2008; Jackson et al. 2006; 2009) and ANNs (e.g., Jones et al. 1999; Shi  
2001; Roberts et al. 2010). ANNs are nonlinear models (or transfer functions) that are trained to  
extract hidden structures and relationships in data, have gained broad applications to retrieving  
various geophysical parameters (Thiria et al. 1993; Krasnopolsky et al. 1995). The types of  
model most often used by ANNs are the logistic sigmoid function and the hyperbolic tangent  
function (a tanh function), both of which feature a characteristic S-shaped curve.

The  $T_b-q_a$  and  $T_b-T_a$  relations (Figures 4-5) are dependent of the thermodynamical  
regimes of the near-surface properties (Esbensen et al. 1993). The relations in the warm/humid  
regime not only depart from the relations in the cold/dry regime but also differ in linearity and  
sensitivity. In this case, an S-shaped mathematical function is not able to capture the complexity  
of the relationships. Special treatment needs to be given for the cold/dry regime at higher  
latitudes.

## 4.2 A high-latitude enhanced global retrieval algorithm

To better address the regime-shift in the  $T_b-q_a$  and  $T_b-T_a$  relations, we propose a three-  
step retrieval approach. The first step is to construct a global model, the second step to construct  
a model for the high-latitude cold/dry regime, and the third step to obtain a high-latitude  
enhanced global retrieval algorithm through merging the two models. The retrieval model is  
based on the second-order polynomial regression and the formulation can be expressed as  
follows:

$$q_a = \sum_m^4 (a_{1,0} + a_{1,m} T b_m + b_{1,m} (T b_m)^2) \quad (1)$$

323 
$$T_a = \sum_m^4 (a_{2,0} + a_{2,m} T b_m + b_{2,m} (T b_m)^2) \quad (2)$$

324 where  $m=1,..4$  denotes the four channels (19v, 22v, 37v, and 52v GHz), and  $a$  and  $b$  are the  
 325 polynomial coefficients for regressing  $Tb$  from the four channels to  $q_a$  and  $T_a$ , respectively. All  
 326 coefficients were determined by the 125 buoy time series in 2010, except for the SOFS buoy  
 327 where the period of March 2010 to February 2011 was used (Table 3).

328 The three-step procedure is executed as follows. Equations (1)-(2) are used for both the  
 329 global model (hereafter GM; Step 1) and the high-latitude model (hereafter HLM; Step 2), and  
 330 the only difference between the two models is the training of the polynomial coefficients. For the  
 331 GM, the 125 buoy time series in 2010 were all used, while for the HLM, only four buoy time  
 332 series were taken. The four buoys are SOFS, OSP, NDBC 46075 and 46085 (Table 3) that are  
 333 located poleward of 40° latitude. The coefficients  $a$  and  $b$  that were trained for the two sets of  
 334 models are listed in Table 4.

335 Once the two models are obtained, the next step (Step 3) is to produce two sets of  $q_a$  and  
 336  $T_a$  daily mean fields that correspond to the respective GM and HLM. The two sets of daily fields  
 337 are then merged over the transition zones depicted by the scatter diagrams (Figures 4-5). The  
 338 transition zone occurs around 8-10 g kg<sup>-1</sup> for  $q_a$ , and 14-17°C for  $T_a$ . Hence, the three-step  
 339 approach can be designed as follows.

340 
$$x = \begin{cases} x(\text{GM}), & \text{if } x \geq xl \\ x(\text{HLM}), & \text{if } x \leq xu \\ x(\text{GM}) \times \alpha + x(\text{HLM}) \times (1 - \alpha), & \text{if } xl \leq x \leq xu \end{cases} \quad (3)$$

341 where  $x$  denotes  $q_a$  or  $T_a$ . We define  $\alpha = (\bar{x} - xl)/(xu - xl)$ , where  $\bar{x}$  is the average of  $x(\text{GM})$  and  
 342  $x(\text{HLM})$ , and  $xu$  ( $xl$ ) is the upper (lower) bound of the transition zone. A flowchart of the three-  
 343 step approach is shown (Figure 6).

344 Production of the daily-mean  $q_a$  and  $T_a$  fields on 01 January 2010 is illustrated (Figures  
345 7a-f) to provide some insights on how the three-step approach is used. On each day, two sets of  
346  $q_a$  and  $T_a$  fields are produced on each day in correspondence to the GM and HLM, respectively,  
347 but neither field is used on the global scale. The GM-based  $q_a$  and  $T_a$  are cut off at the lower  
348 bound of the transition zone, which is set at  $8 \text{ g kg}^{-1}$  for  $q_a$  and  $14^\circ\text{C}$  for  $T_a$  (Figures 7a,d). The  
349 HLM-based estimates are cut off at the upper bound of the transition zone, which is set at  $10 \text{ g}$   
350  $\text{kg}^{-1}$  for  $q_a$  and  $17^\circ\text{C}$  for  $T_a$  (Figures 7b,e). Using Eq.(3), the two sets of estimates are combined  
351 over the transition zone, leading to the merged global daily-mean  $q_a$  and  $T_a$  fields (Figures 7c,f).

352

### 353 4.3 Assessment of the $q_a$ and $T_a$ estimates in the extratropical oceans

354 Our use of the three-step approach aims to improve the estimates of  $q_a$  and  $T_a$  in the less  
355 humid and less warm extratropical region, where one Tb retrieval can fit into both GM and HLM  
356 (Figures 4-5). To assess the improvement made by the three-step approach, we evaluated the  $q_a$   
357 and  $T_a$  retrievals produced at two buoy sites, OSP ( $145^\circ\text{W}$ ,  $50^\circ\text{N}$ ) and KEO ( $144.6^\circ\text{E}$ ,  $32.4^\circ\text{N}$ )  
358 (Figures 8–11). At each site, buoy measurements were a reference for three sets of  $q_a$  and  $T_a$  time  
359 series: those derived from the GM, the HLM, and the merge of the two. Station OSP is located in  
360 the higher latitude cold/dry regime, where buoy measured  $q_a$  was mostly below  $10 \text{ g kg}^{-1}$ , which  
361 is the upper bound of the transition zone (Figure 8). It can be seen that the GM does not work  
362 well at this site, where the  $q_a(\text{GM})$  time series is weakly underestimated in the drier regime ( $q_a <$   
363  $8 \text{ g kg}^{-1}$ ) between Days 1 and 120 and largely overestimated in the more humid regime ( $q_a > 8 \text{ g}$   
364  $\text{kg}^{-1}$ ) between Days 150 and 250. By comparison, the HLM works better. The  $q_a(\text{HLM})$  time  
365 series (Figure 8b) has an overall good performance against buoy time series except for the period  
366 (Days 150–250) when  $q_a$  gets into the transition zone (i.e.  $q_a > 8 \text{ g kg}^{-1}$ ). Following the three-step

367 approach outlined in Eq.(3), we used  $q_a(\text{HLM})$ , not  $q_a(\text{GM})$ , for  $q_a < 8 \text{ g kg}^{-1}$ , and combined the  
368 two sets of estimates for  $q_a \geq 8 \text{ g kg}^{-1}$ . The resultant  $q_a$  time series (Figure 8c) represents an  
369 improvement over both  $q_a(\text{HLM})$  and  $q_a(\text{GM})$ .

370 The  $T_a$  time series at Station OSP was produced in a similar manner:  $T_a(\text{GM})$  (Figure 9a)  
371 is not used except for  $T_a > 14^\circ\text{C}$ , where it is combined with  $T_a(\text{HLM})$  (Figure 9b) to produce an  
372 improved  $T_a$  in the transition zone (Figure 9c). Clearly, the GM and HLM perform well in each  
373 designated regime, but neither of them are desirable in the transition zone. When the two models  
374 are combined, they do lead to improved  $q_a$  and  $T_a$  estimates over the full range of values.

375 The climate at the KEO buoy site is different, as the buoy is located in a western  
376 boundary current region. In 2010, buoy measurements were available from Days 100 to 280,  
377 during which  $q_a$  was predominantly greater than  $8 \text{ g kg}^{-1}$  (Figure 10a). In this humid regime,  
378  $q_a(\text{HLM})$  is poorly produced while  $q_a(\text{GM})$  performs well (Figures 10a–b), and the final  $q_a$  is  
379 estimated primarily by the GM according to Eq.(3). It is seen that HLM is nonresponsive for  $q_a$   
380 greater than  $10 \text{ g kg}^{-1}$  (Figure 10b), because the HLM is trained by four buoys located in the  
381 cold/dry regime. Hence, the HLM works only in the dry/cold regime, and has no skill in the  
382 warm/humid regime.

383

#### 384 4.4 Treatments for SSM/I-based retrievals for the pre-AMSU period

385 AMSU-A was available only after October 1998 (Table 2), and so the retrieval of  $q_a$  and  
386  $T_a$  for the pre-AMSU period needs to be obtained from the SSM/I sensors (Figure 2). The  
387 second-order polynomial fitting algorithms in Eqs. (1)-(2) are then revised as follows:

$$388 \quad q_a = \sum_m^3 (a_{1,0} + a_{1,m} T b_m + b_{1,m} (T b_m)^2) \quad (4)$$

389 
$$T_a = \sum_m^3 (a_{2,0} + a_{2,m}Tb_m + b_{2,m}(Tb_m)^2) + a_{2,SST}SST + b_{2,SST}(SST)^2 \quad (5)$$

390 where  $m=1,2,3$  denotes the three SSM/I channels (19v, 22v, and 37v). Compared to Eqs. (1)-(2),  
 391 the main difference is the inclusion of SST in the  $T_a$  retrieval model (Eq. (5)). The use of SST  
 392 serves two purposes. One is to increase the daily coverage of SSM/I sensors and the other is to  
 393 improve the accuracy of the SSM/I-based  $T_a$  retrievals (e.g. Jackson and Wick 2010). The  
 394 algorithm was trained by the same set of buoy time series in 2010 but excluding AMSU-A Tb in  
 395 the algorithm (Figure 6). The new set of coefficients is provided in Table 5.

396 The retrievals derived from SSM/I only sensors might differ from those derived from the  
 397 combined use of SSM/I and AMSU-A. To address this issue, two sets of retrievals were  
 398 examined, with one produced using the SSM/I+AMSU-A and the other using SSM/I only  
 399 algorithms. The mean differences between the two sets of retrievals for the three years 2000 –  
 400 2002 were shown (Figure 11). For  $q_a$  (Figures 11a,b,c), the differences between the two mean  
 401 fields are distributed in zonal bands with alternating signs. Compared to  $q_a(\text{SSMI})$ ,  
 402  $q_a(\text{SSMI+AMSU-A})$  tends to be lower (i.e. drier) in the mid-latitudes (25–45° North and South)  
 403 and higher (i.e. wetter) in the tropical and higher latitudes. In addition, in the coastal regions off  
 404 California, Peru, and Benguela, the differences between  $q_a(\text{SSMI+AMSU-A})$  and  $q_a(\text{SSMI})$  are  
 405 particularly pronounced, exceeding  $0.5 \text{ g kg}^{-1}$ . For  $T_a$  (Figures 11e,f,g), the pattern of the  
 406 differences between  $T_a(\text{SSMI+AMSU-A})$  and  $T_a(\text{SSMI})$  shows similar spatial structure.

407 For both  $q_a$  and  $T_a$ , the spatial pattern of the differences has only a slight year-to-year  
 408 variation. The time series comparison (Figure 12) shows that the gap between the SSM/I only  
 409 and the SSM/I+AMSU-A retrievals is essentially near-constant for the overlapping 2000-2002  
 410 period. This suggests that the mean difference pattern averaged over the three-year period  
 411 (Figures 11d,h) could be used as a reference to level the mean difference of the pre-AMSU

412 retrievals. The adjustment enables the merge of the pre-AMSU period to produce an 11-sensor  
413 based time series for  $q_a$  and  $T_a$  retrievals from 1988 to 2016. The 29-year averaged global  
414 distribution of the retrieved  $q_a$  and  $T_a$  in January, July, and annual mean (Figure 13) shows the  
415 seasonal contrast of the warm/humid regime in the tropics and the cold/dry regime at higher  
416 latitudes.

417

## 418 **5. Error statistics based on 147 buoys**

419 The buoy time series measurements served two tasks in developing the three-step  
420 retrieval approach: training the empirical relationships prescribed in the retrieval algorithms  
421 (Eqs.(1)-(5)), and validating the  $q_a$  and  $T_a$  retrievals. The first task used 125 buoy time series  
422 collected in 2010, and the second task used 147 independent buoys outside 2010 (Figure 1). To  
423 provide a complete assessment of the  $q_a$  and  $T_a$  daily global fields retrieved from 11 sensors over  
424 the 29-year period, the 147 buoy time series in all available periods are used to evaluate the  
425 statistical properties of the two retrieved products. Summary plots of the buoy-based statistical  
426 properties of the retrieved  $q_a$  and  $T_a$  daily products were constructed (Figures 14-15).

427 The mean retrieved-minus-buoy differences, which are a measure of bias in products,  
428 were constructed at the 147 buoy locations by averaging over the available measurement periods  
429 at each location (Figures 14a-b). The bias in  $q_a$  is generally small, within  $\pm 0.5 \text{ g kg}^{-1}$  at most sites,  
430 including the eastern equatorial Pacific, the south Indian Ocean, the North Atlantic, and the  
431 higher Northern and Southern latitudes. Large mean differences, with magnitude exceeding  $\pm 0.5$   
432  $\text{g kg}^{-1}$ , occur in regions of the equatorial central Pacific and Atlantic Oceans, and also the Bay of  
433 Bengal. These large differences are associated with a highly humid regime where  $q_a$  is usually  
434 greater than  $18 \text{ g kg}^{-1}$  (Figure 13a). By comparison, the bias in  $T_a$  is small, within  $\pm 0.3^\circ\text{C}$ , at

435 almost all locations. The standard deviations (STD) of daily differences between retrieved and  
436 measured values are generally in the range of 0.5–1.0 g kg<sup>-1</sup> for  $q_a$  and 0.3–0.5°C for  $T_a$  (Figures  
437 14c-d). The correlation coefficients between retrieved and measured daily  $q_a$  time series are high,  
438 greater than 0.8 at all locations. The correlation is even higher for  $T_a$ , exceeding 0.9 at most sites  
439 (Figures 14e-f).

440 The overall statistical properties of the retrieved  $q_a$  and  $T_a$  daily values at all buoy sites  
441 are summarized in two scatter plots that were constructed from a total of 475,717 collocations  
442 (Figures 15a-b). The mean differences (biases) of the retrieved  $q_a$  and  $T_a$  are -0.29 g kg<sup>-1</sup> and -  
443 0.13°C, respectively. The STD differences of the retrieved  $q_a$  and  $T_a$  are 0.77 g kg<sup>-1</sup> and 0.50°C,  
444 respectively. The root-mean-square (rms) differences are 0.82 g kg<sup>-1</sup> for the retrieved  $q_a$  and  
445 0.51°C for the retrieved  $T_a$ . The respective correlation coefficients with the buoy counterparts are  
446 high, 0.94 for  $q_a$  and 0.98 for  $T_a$ .

447

## 448 **6. Summary and conclusions**

449 This study uses buoy measurements to show that the Tb- $q_a$  and Tb- $T_a$  relations differ  
450 between the warm/humid tropics and the cold/dry high latitudes and to develop new retrieval  
451 algorithms to address the regime dependence. It is found that the Tb- $q_a$  and Tb- $T_a$  relations are  
452 structured along two distinct, near-linear bands, with a primary band in the warm/humid regime  
453 and a secondary (weaker) band in the cold/dry regime. The step-like transition (or separation)  
454 between the two regimes occurs at 8–10 g kg<sup>-1</sup> for  $q_a$  and 14–17°C for  $T_a$ . The evidence suggests  
455 that one algorithm may not be sufficient to extract  $q_a$  and  $T_a$  from Tb in all regimes. Therefore,  
456 we propose to add a high-latitude enhancement to the global algorithm so that the  $q_a$  and  $T_a$   
457 retrievals in the dry/cold regime can be specifically addressed. This leads to the development of a

458 three-step retrieval approach. The first step is to construct a global model, the second step to  
459 construct a model for the high-latitude cold/dry regime, and the third step to merge the two  
460 models to create a high-latitude enhanced global retrieval algorithm. Both the global and the  
461 high-latitude retrieval models are based on the second-order polynomial regression, and the  
462 difference between the two models is how the regression coefficients are trained. Buoy  
463 measurements in 2010 are used as the training datasets. The global model is trained with 125  
464 buoy time series that are available in 2010, and the high-latitude model is trained with 4 buoys  
465 that are located poleward of 45° latitude north and south. The merge of the two models is  
466 conducted in the respective transition zone for  $q_a$  and  $T_a$ .

467         The new algorithms are applied to 11 microwave sensors from SSM/I, SSMIS, and  
468 AMSU-A between 1988 and 2016. Since AMSU-A was not available before 1998, the  $q_a$  and  $T_a$   
469 retrievals based on SSM/I only are slightly higher than those retrievals derived from  
470 SSM/I+AMSU. Our experiments show that the difference pattern has little change from year to  
471 year, and hence an ensemble mean difference pattern is applied to level down the  $q_a$  and  $T_a$   
472 retrievals before 1998.

473         The buoy time series measurements served two tasks in developing the three-step  
474 retrieval approach: training the empirical relationships prescribed in the retrieval algorithms and  
475 validating the  $q_a$  and  $T_a$  retrievals. The first task used 125 buoy time series collected in 2010, and  
476 the second task used 22 independent buoys that were deployed either before or after 2010. To  
477 provide a fuller assessment of the  $q_a$  and  $T_a$  daily global fields retrieved from 11 sensors over the  
478 29-year period, the 147 buoy time series in all available periods are used to evaluate the  
479 statistical properties of the two retrieved products. On the basis of the 475,717 buoy collocations

480 during the 29-year period, the retrieved  $q_a$  and  $T_a$  have root-mean-square differences of 0.82 g  
481  $\text{kg}^{-1}$  and  $0.51^\circ\text{C}$ , respectively and a mean bias of  $-0.29 \text{ g kg}^{-1}$  and  $-0.13^\circ\text{C}$ , respectively.

482 As expected, the global algorithm with the high-latitude enhancement shows improved  $q_a$   
483 and  $T_a$  retrievals at high latitudes. Nevertheless, the  $T_b$ - $q_a$  and  $T_b$ - $T_a$  relations are more complex  
484 than we could cover in this study. The  $T_b$ - $q_a$  and  $T_b$ - $T_a$  plateaus at very warm ( $T_a > 26^\circ\text{C}$ ) and  
485 very humid ( $q_a > 20 \text{ g kg}^{-1}$ ) conditions need to be further investigated and better represented in  
486 the retrieval algorithm. However, these conditions are generally associated with tropical  
487 convective activities. As pointed out by Esbensen et al. (1993), the Liu method (1986) in the  
488 tropics and the storm-tracked regions may not work in the same way as in the middle and high  
489 latitudes because in regions of active convection, significant amounts of water vapor can exist  
490 aloft where it is acted upon by processes that are less correlated with the humidity at the near-  
491 surface level. Whether there are ways to improve the  $q_a$  and  $T_a$  retrievals in the convective  
492 regime are yet to be fully determined.

493

## 494 **Acknowledgements**

495 The project is sponsored by the NOAA Ocean Observation and Monitoring Division (OOMD)  
496 under grant NA14OAR4320158. We thank the following data sources for providing the data  
497 used in this study. SSMI and SSMS were downloaded from Remote Sensing Systems  
498 (<http://www.ssmi.com/>) The AMSU-A was acquired from NOAA's National Climatic Data  
499 Center (<http://www.ncdc.noaa.gov>). Buoy measurements from TAO, PIRATA, and RAMA  
500 programs were downloaded from <http://pmel.noaa.gov>, and those from ARC, KEO and OSP  
501 were from <http://www.pmel.noaa.gov/ocs>. The WHOI buoys (Arabian Sea, ASREX91,  
502 ASREX93, Bay of Bengal, CLIMODE, CMO, COARE, MLML91, NTAS, PACS, SESMOOR,

503 SMILE, Stratus, Subduction, WHOTS) were from <http://uop.who.edu>. The SOFS mooring is  
504 part of the Australian Integrated Marine Observing System (IMOS) with data available from  
505 <https://portal.aodn.org.au>. The OOI SO and Argentine buoys were from  
506 <https://ooinet.oceanobservatories.org>. We thank Bob Weller and Nan Galbraith for providing the  
507 OOI Irminger Sea buoy measurements.

508 **References**

- 509 Berry, D. I., and E. C. Kent (2009), A new air-sea interaction dataset from ICOADS with  
510 uncertainty estimates. *Bull. Am. Meteorol. Soc.*, **90**(5), 645–656.
- 511 Bentamy, A., K. B. Katsaros, A. M. Mestas-Nunoz, W. M. Drennan, E. B. Forde, and H. Roquet  
512 (2003), Satellite estimates of wind speed and latent heat flux over the global oceans. *J. Clim.*,  
513 **16**, 637–656.
- 514 Boulès, B., R. Lumpkin, M.J. McPhaden, F. Hernandez, P. Nobre, E. Campos, L. Yu, S. Planton,  
515 A. Busalacchi, A.D. Moura, J. Servain, and J. Trotte (2008), The PIRATA Program: History,  
516 accomplishments, and future directions. *Bull. Am. Meteorol. Soc.*, **89**, 1111-1125.
- 517 Bretherton, C. S., M. E. Peters, and L. E. Back (2004), Relationships between water vapor path  
518 and precipitation over the tropical oceans, *J. Clim.*, **17**, 1517–1528.
- 519 Chou S.-H., R. M. Atlas, C-L. Shie, and J. Ardizzone (1995), Estimates of surface humidity and  
520 latent heat fluxes over oceans from SSM/I Data, *Mon. Weather Rev.*, **123**, 2405-2425.
- 521 Colbo, K. and R. A. Weller (2009), The accuracy of the IMET sensor package in the subtropics.  
522 *J. Atmos. Ocean. Technol.*, **26**(9), 1867-1890.
- 523 Cronin, M. F., C. Meinig, C. L. Sabine, H. Ichikawa, and H. Tomita (2008), Surface mooring  
524 network in the Kuroshio Extension. *IEEE Systems Special Issue on GEOSS*, **2**(3), 424-430.
- 525 Curry, J. A., A. Bentamy, M.A. Bourassa, D. Bourras, E.F. Bradley, M. Brunke, S. Castro, S.H.  
526 Chou, C.A. Clayson, W.J. Emery, L. Eymard, C.W. Fairall, M. Kubota, B. Lin, W. Perrie, R.A.  
527 Reeder, I.A. Renfrew, W.B. Rossow, J. Schulz, S.R. Smith, P.J. Webster, G.A. Wick, and X.  
528 Zeng (2004), SEAFLUX. *Bull. Am. Meteor. Soc.*, **85**, 409-424.
- 529 Dai, A. (2006), Recent climatology, variability, and trends in global surface humidity. *J.*  
530 *Clim.*, **19**, 3589–3606.

531 Esbensen, S. K., D. B. Chelton, D. Vockers, and J. Sun (1993), An analysis of errors in Special  
532 Sensor Microwave Imager evaporation estimates over the global oceans. *J. Geophys. Res.*, **98**,  
533 7081-7101.

534 Fairall, C. W., E. F. Bradley, J. E. Hare, A. A. Grachev, and J. B. Edson (2003), Bulk  
535 parameterization of air-sea fluxes: Updates and verification for the COARE algorithm. *J.*  
536 *Clim.*, **16**, 571–591.

537 Goldberg, M. D.( 1999), Generation of retrieval products from AMSU-A: Methodology and  
538 validation. *10th International TOVS Study Conference*, Boulder, Colorado, 27 January – 2  
539 February.

540 Hansen, J., A. Lacis, D. Rind, G. Russell, P. Stone, I. Fung, R. Ruedy, and J. Lerner (1984),  
541 *Climate sensitivity: Analysis of feedback mechanisms*. In: *Climate Processes and Climate*  
542 *Sensitivity*, J. E. Hansen and T. Takahashi, eds., Washington, D.C., American Geophysical  
543 Union. pp. 130-163.

544 Held, I.M. and B.J. Soden, 2006: [Robust Responses of the Hydrological Cycle to Global](#)  
545 [Warming](#). *J. Climate*, **19**, 5686–5699, <https://doi.org/10.1175/JCLI3990.1>

546 Hollinger, J.P., J. L. Peirce, and G. A. Poe (1990), SSM/I Instrument Evaluation. *IEEE Trans.*  
547 *Geosci. Remote Sens.*, **28**(5), 781–790.

548 Hsu, S. A., and B. W. Blanchard (1989), The relationship between total precipitable water and  
549 surface-level humidity over the sea surface: A further evaluation. *J. Geophys. Res.*, **94**, 14,539-  
550 14,545.

551 Jackson, D.L., G.A. Wick, and J.J. Bates( 2006), Near-surface retrieval of air temperature and  
552 specific humidity using multi-sensor microwave satellite observations. *J. Geophys. Res.* **111**,  
553 D10306, doi:10.1029/2005JD006431.

554 Jackson, D. L., G. A. Wick, and F. R. Robertson (2009), Improved multisensor approach to  
555 satellite-retrieved nearsurface specific humidity observations. *J. Geophys. Res.*, **114**, 1-13,  
556 doi:10.1029/2008JD011341.

557 Jackson, D.L. and G. A. Wick (2010), Near-surface air temperature retrieval derived from  
558 AMSU-A and sea surface temperature observations. *J. Atmos. Ocean. Technol.*, **27**, 1769-1776.

559 Jin, X., L. Yu, D. L. Jackson, and G. A. Wick, (2015), An improved near-surface specific  
560 humidity and air temperature climatology for the SSM/I satellite period. *J. Atmos. Oceanic  
561 Technol.*, **32**, 412–433, doi: <http://dx.doi.org/10.1175/JTECH-D-14-00080.1>.

562 Jones, C., P. Peterson, and C. Gautier (1999), A new method for deriving ocean surface specific  
563 humidity and air temperature: An artificial neural network approach. *J. Appl. Meteorol.*, **38**,  
564 1229–1245.

565 Kamphaus, R., M. Cronin, C. Sabine, S. Emerson, C. Meinig, and M. Robert (2008), New  
566 surface mooring at Station PAPA monitors climate. *PICES Press*, **16**(2), 26-27.

567 Kent, E.; Taylor, P.K. (1996), Accuracy of humidity measurements on ships: Consideration of  
568 solar radiation effects. *J. Atmos. Ocean. Technol.*, **13** (6). 1317-1321.10.1175/1520-  
569 0426(1996)013<1317:AOHMOS>2.0.CO;2

570 Krasnopolsky, V. M., L. C. Breaker, and W. H. Gemmill (1995), A neural network as a nonlinear  
571 transfer function for retrieving surface wind speeds from the special sensor microwave imager.  
572 *J. Geophys. Res.*, **100**, 11 033–11 045.

573 Kubota, M., and T. Hihara (2008), Retrieval of surface air specific humidity over the ocean using  
574 AMSR-E measurements. *Sensors*, **8**, 8016–8026, doi:10.3390/s8128016.

575 Liu, W. T. (1986), Statistical relation between monthly precipitable water and surface-level  
576 humidity over global oceans. *Mon. Weather Rev.*, **114**, 1591–1602.

577 Liu, W. T. (1988), Moisture and latent heat flux variabilities in the tropical Pacific derived from  
578 satellite data. *J. Geophys. Res.*, **93**, 6749–6760.

579 Liu, W.T., and P.P. Niiler (1984), Determination of monthly mean humidity in the atmospheric  
580 surface layer over oceans from satellite data. *J. Phys. Oceanogr.*, **14**, 1451-1457.

581 Liu, W.T., W. Tang, and P.P. Niiler (1991), Humidity profiles over oceans. *J. Clim.*, **4**, 1023-  
582 1034.

583 Lorenz, D. J., E. T. DeWeaver, and D. J. Vimont (2010), Evaporation change and global  
584 warming: The role of net radiation and relative humidity, *J. Geophys. Res.*, **115**, D20118,  
585 doi:10.1029/2010JD013949.

586 Manabe, S., and R. T. Wetherald (1967), Thermal equilibrium of atmosphere with a given  
587 distribution of relative humidity, *J. Atmos. Sci.*, **24**, 241–259.

588 McPhaden, M. J., and coauthors (1998), The Tropical Ocean-Global Atmosphere observing  
589 system: A decade of progress, *J. Geophys. Res.*, **103**(C7), 14,169–14,240,  
590 doi:10.1029/97JC02906.

591 McPhaden, M. J., G. Meyers, K. Ando, Y. Masumoto, V. S. N. Murty, M. Ravichandran, F.  
592 Syamsudin, J. Vialard, L. Yu, and W. Yu (2009), RAMA: The Research Moored Array for  
593 African-Asian-Australian Monsoon Analysis and Prediction. *Bull. Am. Meteor. Soc.*, **90**, 459-  
594 480.

595 Moyer, K. A. and R. A. Weller (1997), Observations of surface forcing from the Subduction  
596 Experiment: A comparison with global model products and climatological data sets. *J. Clim.*, **10**,  
597 2725-2742.

598 Payne, R. E., K. Huang, R. Weller, H.P. Freitag, M. F. Cronin, M.J. McPhaden, C. Meinig, Y.  
599 Kuroda, N. Ushijima, and R.M. Reynolds (2002), A comparison of buoy meteorological

600 systems. WHOI Tech. Rep. WHOI-2002-10, 67 pp., Woods Hole Oceanogr. Inst., Woods Hole,  
601 Mass.

602 Prytherch, J., E. C. Kent, S. Fangohr, and D. I. Berry (2014), A comparison of SSM/I-derived  
603 global marine surface-specific humidity datasets. *Int. J. Climatol.*, **35**, 2359–2381.  
604 doi:<https://doi.org/10.1002/joc.4150>.

605 Roberts, J. B., C. A. Clayson, F. R. Robertson, and D. L. Jackson (2010), Predicting near-surface  
606 atmospheric variables from Special Sensor Microwave/Imager using neural networks with a  
607 first-guess approach. *J. Geophys. Res.*, **115**, D19113, doi:10.1029/2009JD013099.

608 Schlüssel, P., L. Schanz, and G. Englisch (1995), Retrieval of latent heat flux and longwave  
609 irradiance at the sea surface from SSM/I and AVHRR measurements. *Adv. Space Res.*, **16**(10),  
610 107–116.

611 Schulz, J., P. Schluessel, and H. Grassl (1993), Water vapour in the atmospheric boundary layer  
612 over oceans from SSM/I measurements. *Int. J. Remote Sens.*, **14**, 2773 – 2789.

613 Schulz, E. W., S. A. Josey, and R. Verein (2012), First air-sea flux mooring measurements in the  
614 Southern Ocean, *Geophys. Res. Lett.*, **39**, L16606, doi:10.1029/2012GL052290.

615 Send, U., Weller, R., Wallace, D., Chavez, F., Lampitt, R., Dickey, T., Honda, M., Nittis, K.,  
616 Lukas, R., McPhaden, M. and Feely, R. (2010) "OceanSITES" in *Proc. of OceanObs '09:*  
617 *Sustained Ocean Observations and Information for Society (Vol. 2)*, Venice, Italy, 21-25  
618 September 2009, Hall, J., Harrison, D.E. and Stammer, D., Eds., ESA Publication WPP-306,  
619 doi:10.5270/OceanObs09.cwp.79

620 Sherwood, S. C., R. Roca, T. M. Weckwerth, and N. G. Andronova (2010), Tropospheric water  
621 vapor, convection and climate. *Rev. Geophys.*, **48**, RG2001, doi:10.1029/2009RG000301.

622 Shi, L. (2001), Retrieval of atmospheric temperature profiles from AMSU-A measurement using  
623 a neural network approach. *J. Atmos. Ocean. Technol.*, **18**, 340–347.

624 Shi, L., G. Peng, and J. J. Bates (2012) Surface air temperature and humidity from intersatellite-  
625 calibrated HIRS measurements in high latitudes. *J. Atmos. Ocean. Technol.*, **29**, 3-13,  
626 doi:10.1175/JTECH-D-11-00024.1.

627 Shie, C.-L., K. Hilburn, L. S. Chiu, R. Adler, I-I Lin, E. Nelkin, J. Ardizzone, and S. Gao (2012),  
628 Goddard Satellite-Based Surface Turbulent Fluxes, Daily Grid, version 3. Edited by Andrey  
629 Savtchenko., Greenbelt, MD, USA: Goddard Earth Science Data and Information Services  
630 Center (GES DISC), Accessed Enter User Data Access Date at  
631 doi:10.5067/MEASURES/GSSTF/DATA301.

632 Stephens, G. L. (1990), On the relationship between water vapor over the oceans and sea surface  
633 temperature. *J. Clim.*, **3**, 634–645.

634 Taylor, P. K. (1982), Remote sensing of atmospheric water content and sea surface latent heat  
635 flux. *Proc. Annual Technical Conf. on Remote Sensing and the Atmosphere*, Reading, United  
636 Kingdom, Remote Sensing Society, 265–272.

637 Thiria, S., C. Mejia, F. Badran, and M. Crepon (1993), A neural network approach for modelling  
638 nonlinear transfer functions: Application for wind retrieval from spaceborne scatterometer data.  
639 *J. Geophys. Res.*, **98**, 22 827–22 842.

640 Weller, R. A. and S. P. Anderson (1996), Surface meteorology and air-sea fluxes in the western  
641 equatorial Pacific warm pool during the TOGA Coupled Ocean-Atmosphere Response  
642 Experiment. *J. Clim.*, **9**(8), 1959-1990.

643 Wentz, F.J. (1997), A well-calibrated ocean algorithm for SSM/I. *J. Geophys. Res.*, **102**, C4,  
644 8703-8718.

645 Wentz, F. J. (2013), SSM/I Version-7 Calibration Report. Report number 011012, Remote  
646 Sensing Systems, Santa Rosa, CA, 46 pp.

647 Willett, K. M., P. D. Jones, N. P. Gillett, and P. W. Thorne (2008), Recent changes in surface  
648 humidity: Development of the HadCRUH dataset, *J. Clim.*, **21**, 5364–5383,  
649 doi:10.1175/2008JCLI2274.1.

650 Yu, L., and R. A. Weller (2007), Objectively analyzed air-sea heat fluxes for the global ice-free  
651 oceans (1981-2005). *Bull. Am. Meteor. Soc.*, **88**(4), 527-539

652 Yu, L., 2007. Global variations in oceanic evaporation (1958-2005): The role of the changing  
653 wind speed. *J. Climate*, 20(21), 5376-5390.

654 Yu, L., X. Jin, and R. Weller (2008), Multidecade Global Flux Datasets from the Objectively  
655 Analyzed Air-sea Fluxes (OAFlux) Project: Latent and Sensible Heat Fluxes, Ocean  
656 Evaporation, and Related Surface Meteorological Variables, OAFlux Project Tech. Rep. OA-  
657 2008-01, 64 pp.

658 Zou, C.-Z., and W. Wang (2013), Climate algorithm theoretical basis document (C-ATBD) -  
659 AMSU radiance fundamental climate data record derived from integrated microwave inter-  
660 calibration approach, *Tech. Rep.*, NOAA, Asheville, N. C.

661

662

663 **List of Tables**

664 Table 1. Summary of the Qa/Ta algorithms developed in the past 30 years

665 Table 2. List of satellite sensors used in the study

666 Table 3. List of the 30 buoys that are not associated with TRITON/TAO, PIRATA, and RAMA

667 Table 4. Regression coefficients for Equations (1)-(2)

668 Table 5. Regression coefficients for Equations (4)-(5)

669

670 **Figure captions**

671 Figure 1. Locations of 147 moored surface buoys. The 121 red squares denote that the  
672 measurements made by those buoys in 2010 were used as training datasets for the global model,  
673 while the 4 red squares with black edges located at high latitudes were used as training datasets  
674 for the high latitude model. The 22 blue squares denote that the measurements at these  
675 locations were made either before or after 2010 so that they can be used as independent  
676 validation datasets.

677 Figure 2. Timeline and duration of the 11 sensors used in the study.

678 Figure 3. Daily-mean fields of brightness temperature ( $T_b$ ) on 01 January 2010 observed by  
679 SSMIS F17 channels at (a) 19 GHz, (b) 22 GHz, (c) 37 GHz, and AMSU-A channel at (d) 52  
680 GHz. The daily mean fields are the average of the ascending and descending passes.

681 Figure 4. Scatter diagrams of buoy measured  $q_a$  versus  $T_b$  from SSMIS F17 channels at (a) 19  
682 GHz, (b) 22 GHz, (c) 37 GHz, and AMSU-A channel at (d) 52 GHz. The diagrams are based  
683 on a total of 31,793 tri-collocations between buoy, SSMIS, and AMSU-A that are constructed  
684 in 2010.

685 Figure 5. Same as Figure 4 but for buoy measured  $T_a$ .

686 Figure 6. A flowchart of the three-step procedure that incorporates a high-latitude enhancement  
687 into the global retrieval algorithm.

688 Figure 7. An illustration of how the three-step procedure works using the data generation on 01  
689 January 2010 as an example. The  $q_a$  fields produced by (a) the global model (GM), (b) the  
690 high-latitude model (HLM), and (c) merge of the GM and HLM. The  $T_a$  fields produced by (d)  
691 the global model (GM), (e) the high-latitude model (HLM), and (f) merge of the GM and HLM.

692 Figure 8. Examining the performance of the GM, HLM, and the merged approach for  $q_a$   
693 retrievals using buoy measurements at Ocean Station PAPA 145°W, 50.0°N. Time series  
694 comparison for (a) GM, (c) HLM, and (e) the merged, and the scatter diagrams of buoy versus  
695 (b) GM, (d) HLM, and (f) the merged.

696 Figure 9. Same as Figure 8 but for  $T_a$ .

697 Figure 10. Same as Figure 8 but for  $q_a$  at the KEO site 144.6°E, 32.4°N.

698 Figure 11. Using SSM/I sensors to retrieve  $q_a$  (left) and  $T_a$  (right) with and without AMSU-A.

699 The mean differences between the two  $q_a$  patterns in (a) 2000, (b) 2001, (c) 2002, and (d) the  
700 three-year mean. The mean differences between the two  $T_a$  patterns in (e) 2000, (f) 2001, (g)  
701 2002, and (h) the three-year mean.

702 Figure 12. Annual-mean time series of SSM/I-only retrievals (red line), SSM/I+SSMIS+AMSU  
703 retrievals (black), and the mean-adjusted SSM/I-only retrievals (grey) for (a)  $q_a$  and (b)  $T_a$ .

704 Figure 13. Time-mean fields of the retrieved  $q_a$  in (a) January, (b) July, and (c) annual mean, and  
705 the retrieved  $T_a$  in (d) January, (e) July, and (f) annual mean. The mean fields are constructed  
706 for the period 1988-2016.

707 Figure 14. Statistical properties of the retrieved  $q_a$  and  $T_a$  daily products evaluated at the 147  
708 buoy locations. Retrieved-minus-buoy differences averaged over the available measurement  
709 periods for (a)  $q_a$  and (b)  $T_a$ , the standard deviations of daily retrieved-minus-buoy differences  
710 for (c)  $q_a$  and (d)  $T_a$ , and the correlation coefficient between retrieved and measured daily time  
711 series for (e)  $q_a$  and (f)  $T_a$ .

712 Figure 15. Scatter plots of the retrieved versus observed parameters for (a) specific humidity at  
713 2m ( $q_a$ ) and (b) air temperature ( $T_a$ ) based on buoy time series measurements at 147 locations  
714 for the period 1988 – 2016.

715 Table 1. Summary of the  $Q_a/T_a$  algorithms developed in the past 30 years

Algorithm	Sensors	Retrieval Methodology for $q_a$	Training data	Retrieval Methodology for $T_a$
Liu (1986)		First algorithm to relate $q_a$ to IWV	Radiosonde soundings	N/A
Liu (1988)	SSM/I	N/A	Radiosonde soundings	Obtained from surface mixing ratio assuming a constant relative humidity of 80%
Schulz et al. (1993)	SSM/I	Linear regression using IWV in the lower 500m boundary layer.	Radiosonde soundings	N/A
Chou et al. (1995)	SSM/I	EOF-based approach using IWV in the lower boundary layer.	Radiosonde soundings	N/A
Schluessel et al. (1995)	SSM/I	Linear regression using $T_b$ from five channels (19v, 22v, 37v, 19h, and 37h).	Radiosonde soundings	N/A
Jones et al. (1999)	SSM/I	First neural network approach using SSM/I IWV and NCEP SST.	OISST (NCEP version)	Simultaneously retrieved
Bentamy et al. (2003)	SSM/I	Similar to Schluessel et al. (1995) but using a 4-channel regression (no 37v)	Ship observations	N/A
Kubota and Hihara (2008)	AMSR-E	Similar to Schluessel et al. (1995) but using a 12-channel regression	NCEP and Ship observations	N/A
Shi (2001)	AMSU-A	N/A	NCEP	Neural network approach
Jackson et al. (2006; 2009)	AMSU-A SSM/I SSM/T-2	Multivariate linear regression	Ship Observations	Simultaneously retrieved
Shi et al. (2012)	HIRS	Neural network approach	ECMWF and ships	Simultaneously retrieved
Roberts et al. (2010; 2012)	SSM/I	Neural network approach	Research vessels and buoys	Simultaneously retrieved
This Paper	AMSU-A SSM/I SSMIS	A 4-Channel nonlinear regression with high-latitude enhancement	Buoys	Simultaneously retrieved

716  
717  
718  
719

720  
721  
722  
723

Table 2. List of satellite sensors used in the study

Sensor	Period in use	Channel in use	Swath Width	Daily coverage
SSM/I F08	01/01/88 – 12/31/91	19v 22v 37v	1394 km	74.5%
SSM/I F10	12/31/90 – 08/31/97			
SSM/I F11	12/01/91 – 03/01/00			
SSM/I F13	05/01/95 – 11/01/09			
SSM/I F14	05/01/97 – 12/01/05			
SSM/I F15	12/01/99 – 12/31/05			
SSMIS F17	01/01/07 – 12/31/16	19v, 22v, 37v	1700 km	83.5%
AMSU-A N15	10/01/98 – 12/31/16	52v	2343 km	96.9%
AMSU-A N16	01/01/01 – 12/31/06			
AMSU-A N17	06/01/02 – 12/31/03			
AMSU-A N18	05/02/05 – 12/31/16			

724  
725

Table 3. List of the 30 buoys that are not associated with TRITON/TAO, PIRATA, and RAMA

<b>Buoy</b>	<b>Location</b>	<b>Period used in study</b>
Arabian Sea	61.5°E, 15.5°N	10/16/94 – 10/19/95
ARC	30.0°E, 38.5°S	12/01/10 – 03/08/11
ASREX91	132.0°W, 49.2°N	11/01/91 – 01/06/92
ASREX93	69.7°W, 33.9°N	12/15/93 – 03/23/94
Bay of Bengal	89.5°E, 18.0°N	12/08/14 – 01/29/16
CLIMODE	65.0°W, 38.0°N	11/14/05 – 02/08/07
CMO	70.5°W, 40.5°N	07/31/96 – 06/12/97
TOGA COARE	156.0°E, 1.8°S	10/22/92 – 03/03/93
KEO	144.6°E, 32.4°N	06/16/04 – 12/31/16
MLML91	20.8°W, 59.5°N	04/30/91 – 09/05/91
NTAS	51.0°W, 14.8°N	03/31/01 – 12/31/16
PACS(n)	125.4°W, 9.9°N	04/30/97 – 09/13/98
PACS(s)	124.6°W, 2.8°S	04/21/97 – 09/19/98
PAPA	145.0°W, 50.0°N	06/08/07 – 12/31/16
SESMOOR	61.2°W, 42.5°N	10/18/88 – 03/07/89
SMILE	123.5°W, 39.6°N	11/15/88 – 05/14/89
SOFS	142.0°E, 46.8°S	03/17/10 – 12/24/12
SPURS	38.0°W, 24.6°N	09/14/12 – 09/30/13
Stratus	85.0°W, 20.0°S	10/08/00 – 12/31/16
WHOTS	158.0°W, 22.8°N	09/15/04 – 12/31/16
Subduction	34.0°W, 33.0°N	06/19/91 – 06/20/93
Subduction	22.0°W, 33.0°N	06/19/91 – 06/20/93
Subduction	29.0°W, 25.5°N	06/19/91 – 06/20/93
Subduction	22.0°W, 18.0°N	06/19/91 – 06/20/93
Subduction	34.0°W, 18.0°N	06/19/91 – 06/20/93
OOI SO	89.2°W, 54.4°S	12/17/15 – 11/28/16
OOI Argentine	42.6°W, 42.9°S	11/14/15 – 11/08/16

OOI Irminger Sea	39.5°W, 59.9°N	09/13/14 – 01/25/16
NDBC 46075	160.8°W, 53.9°N	05/08/04 – 12/31/16
NDBC 46085	142.5°W, 55.9°N	05/05/07 – 12/31/16

729  
730  
731  
732  
733  
734  
735

Table 4. Regression coefficients for Equations (1)-(2)

Add one more digit for the highlighted values (i.e. need 5 digits after the decimal point if the integer digit is 0)

<b>Model</b>	<b>A<sub>0</sub></b>	<b>A<sub>19v</sub></b>	<b>A<sub>22v</sub></b>	<b>A<sub>37v</sub></b>	<b>A<sub>52v</sub></b>	<b>B<sub>19v</sub></b>	<b>B<sub>22v</sub></b>	<b>B<sub>37v</sub></b>	<b>B<sub>52v</sub></b>
q <sub>a</sub> (GM)	1423.34	0.46967	0.43401	-0.92292	-11.494	-0.00071	-0.00072	0.00155	0.02336
q <sub>a</sub> (HLM)	-127.10	-0.21113	0.71712	-0.78268	1.1918	0.00062	-0.00139	0.00153	-0.00222
T <sub>a</sub> (GM)	-389.96	0.48775	0.75817	-1.3532	2.8253	-0.00093	-0.00156	0.00265	-0.00463
T <sub>a</sub> (HLM)	-624.73	-1.7726	1.4135	-1.4004	6.1955	0.00459	-0.00299	0.00268	-0.01220

736  
737  
738

739 Table 5. Regression coefficients for Equations (4)-(5)  
 740  
 741

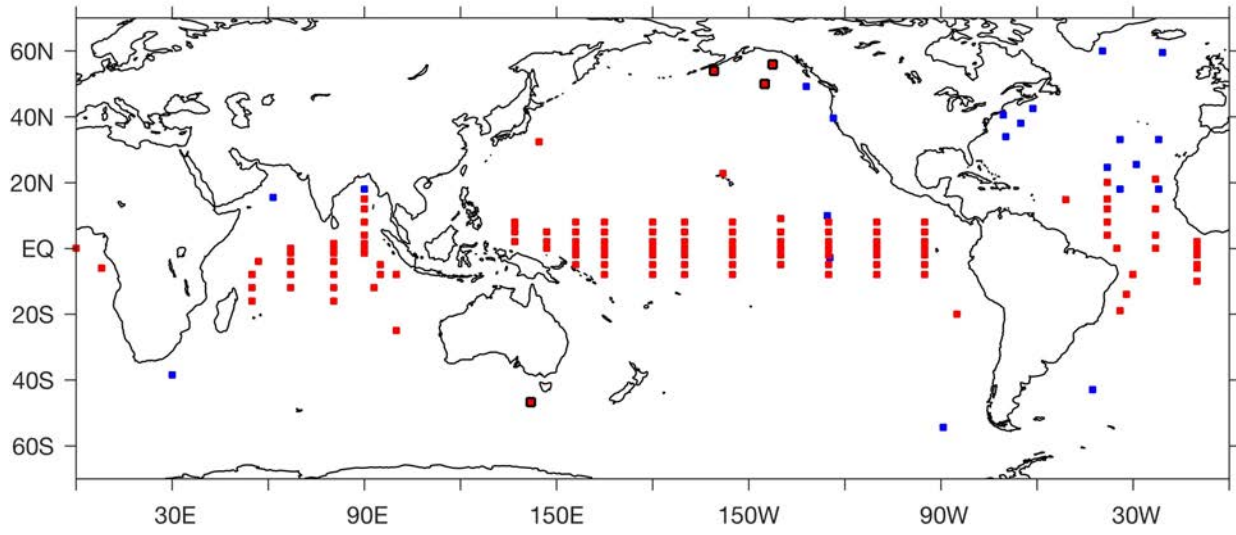
<b>Model</b>	<b>A<sub>0</sub></b>	<b>A<sub>19v</sub></b>	<b>A<sub>22v</sub></b>	<b>A<sub>37v</sub></b>	<b>B<sub>19v</sub></b>	<b>B<sub>22v</sub></b>	<b>B<sub>37v</sub></b>	<b>A<sub>SST</sub></b>	<b>B<sub>SST</sub></b>
q <sub>a</sub> (GM)	20.773	1.0004	0.68113	1.0004	-0.00166	-0.00100	0.00306	N/A	N/A
q <sub>a</sub> (HLM)	36.335	-0.48568	0.93744	-0.4857	0.00123	-0.00180	0.00157	N/A	N/A
T <sub>a</sub> (GM)	-14.114	0.06469	1.4800	-1.4004	0.00003	-0.00293	0.00271	0.36543	0.00989
T <sub>a</sub> (HLM)	170.11	-2.6251	2.0226	-1.2309	0.00660	-0.00433	0.00261	1.2728	- 0.02626

742  
 743

744

745

746



747

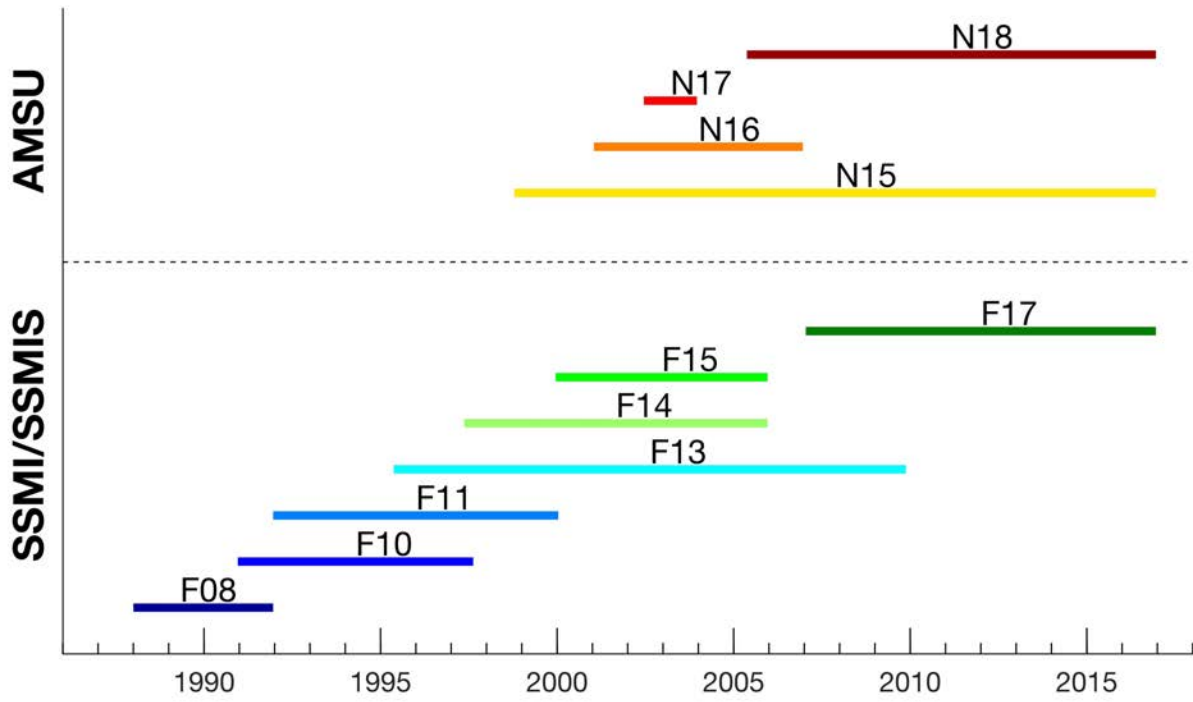
748

749 Figure 1

750

751

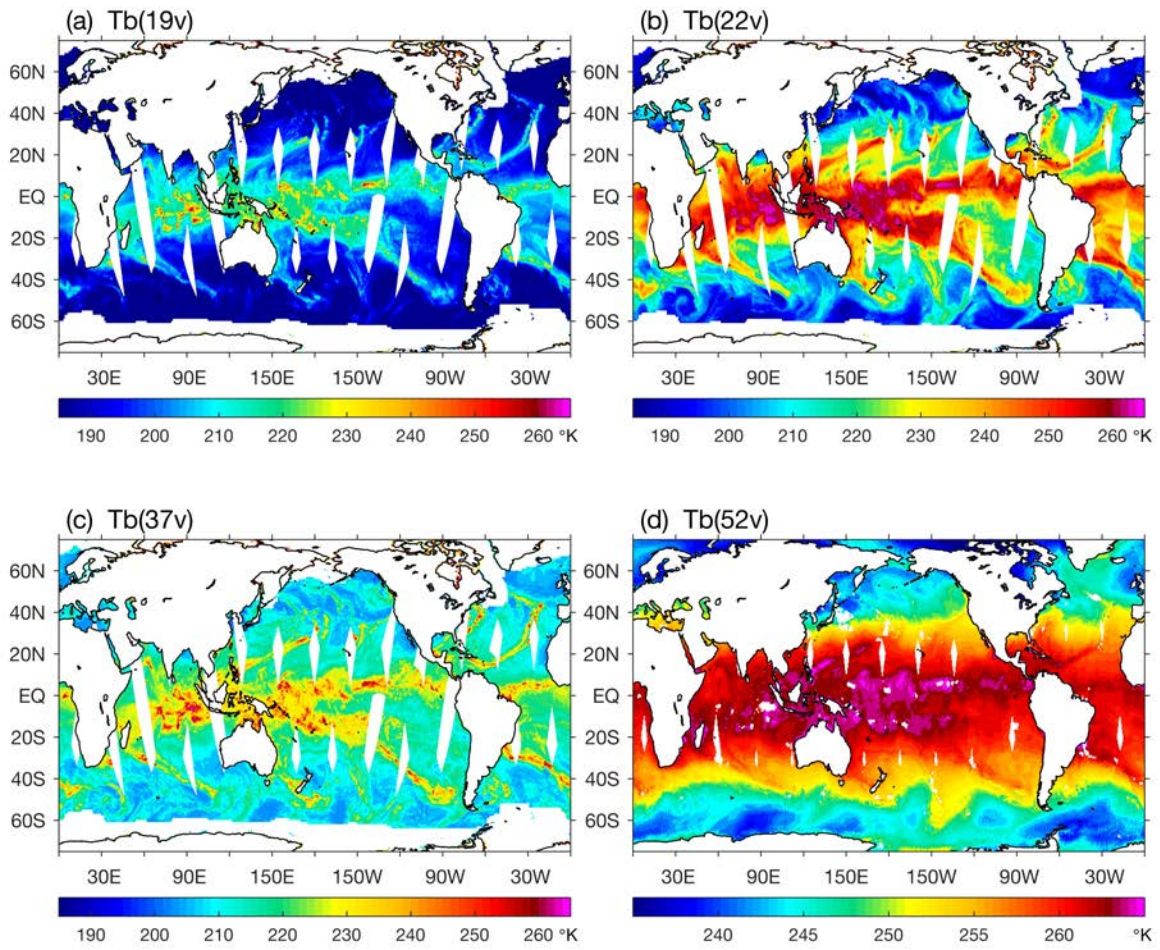
752



753

754

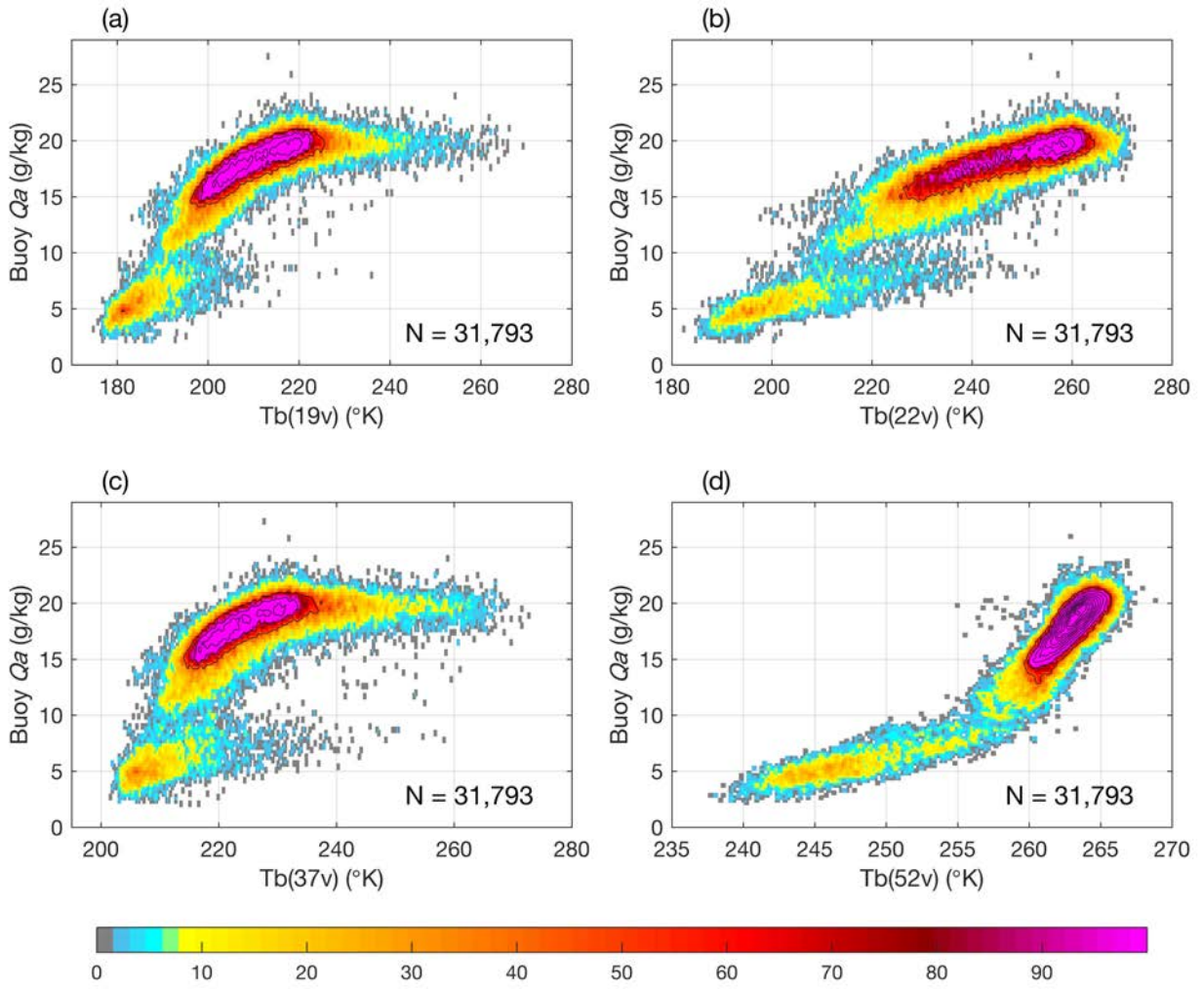
755 Figure 2



756

757 Figure 3

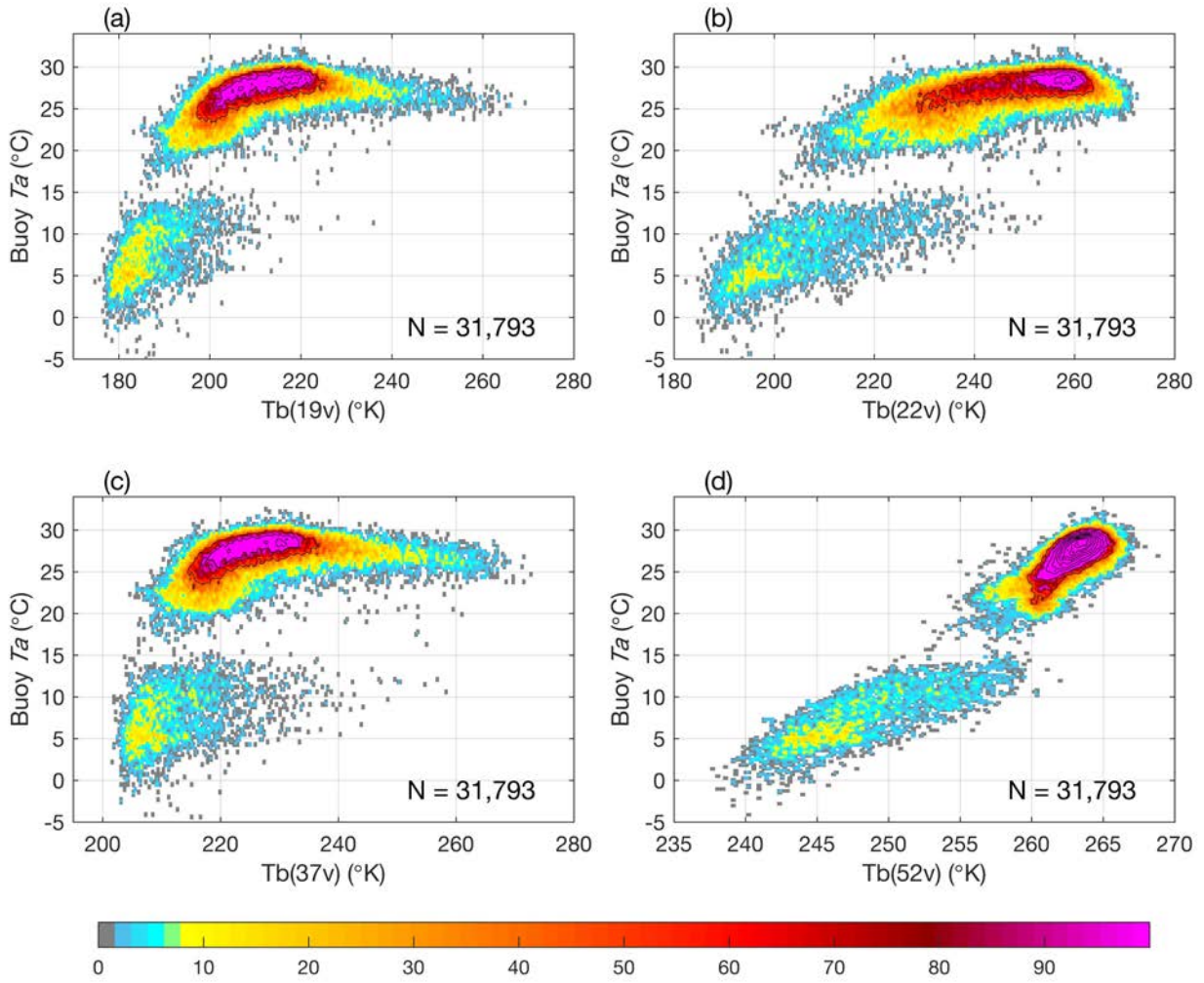
758



759

760

761 Figure 4

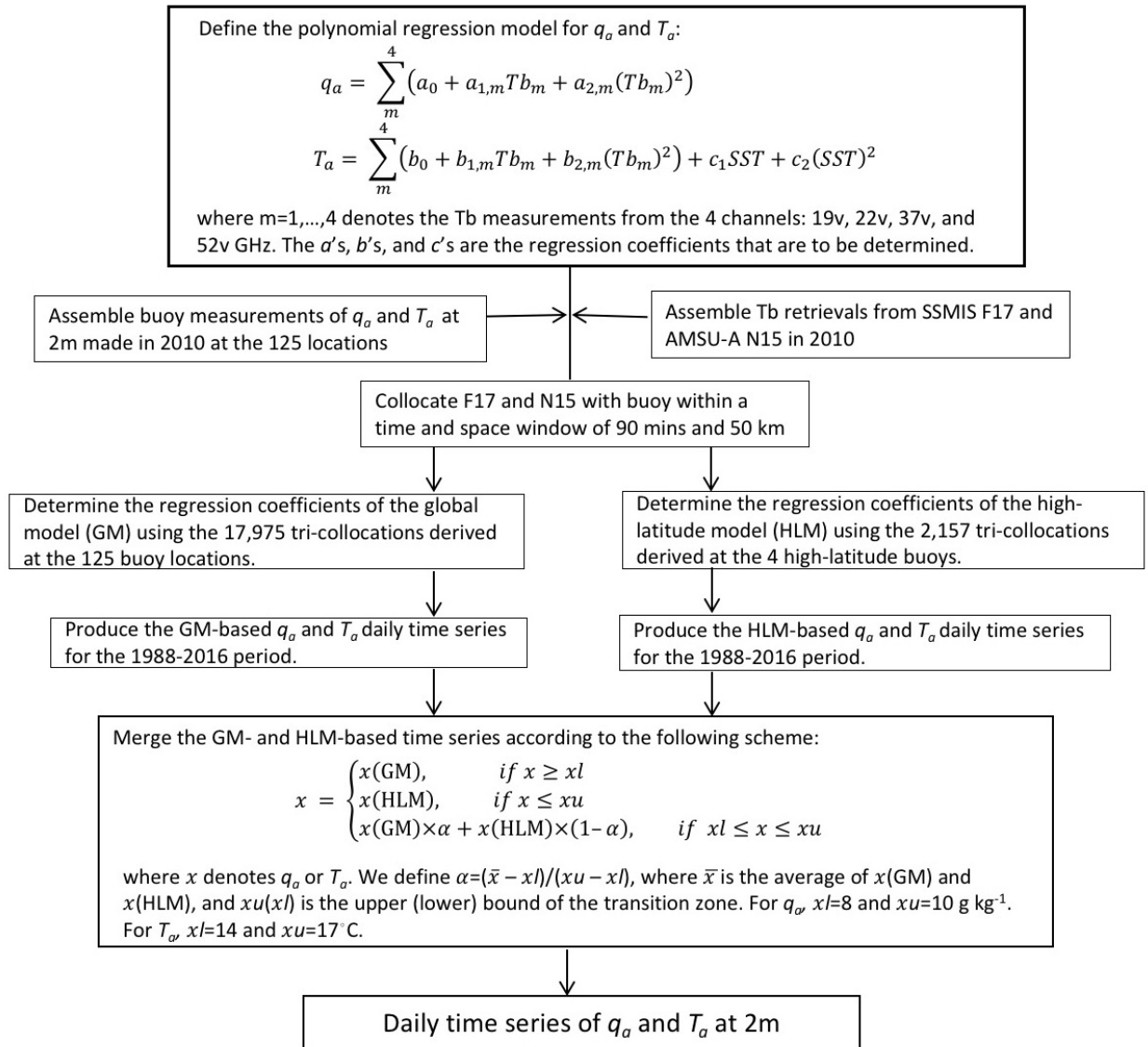


762

763

764 Figure 5

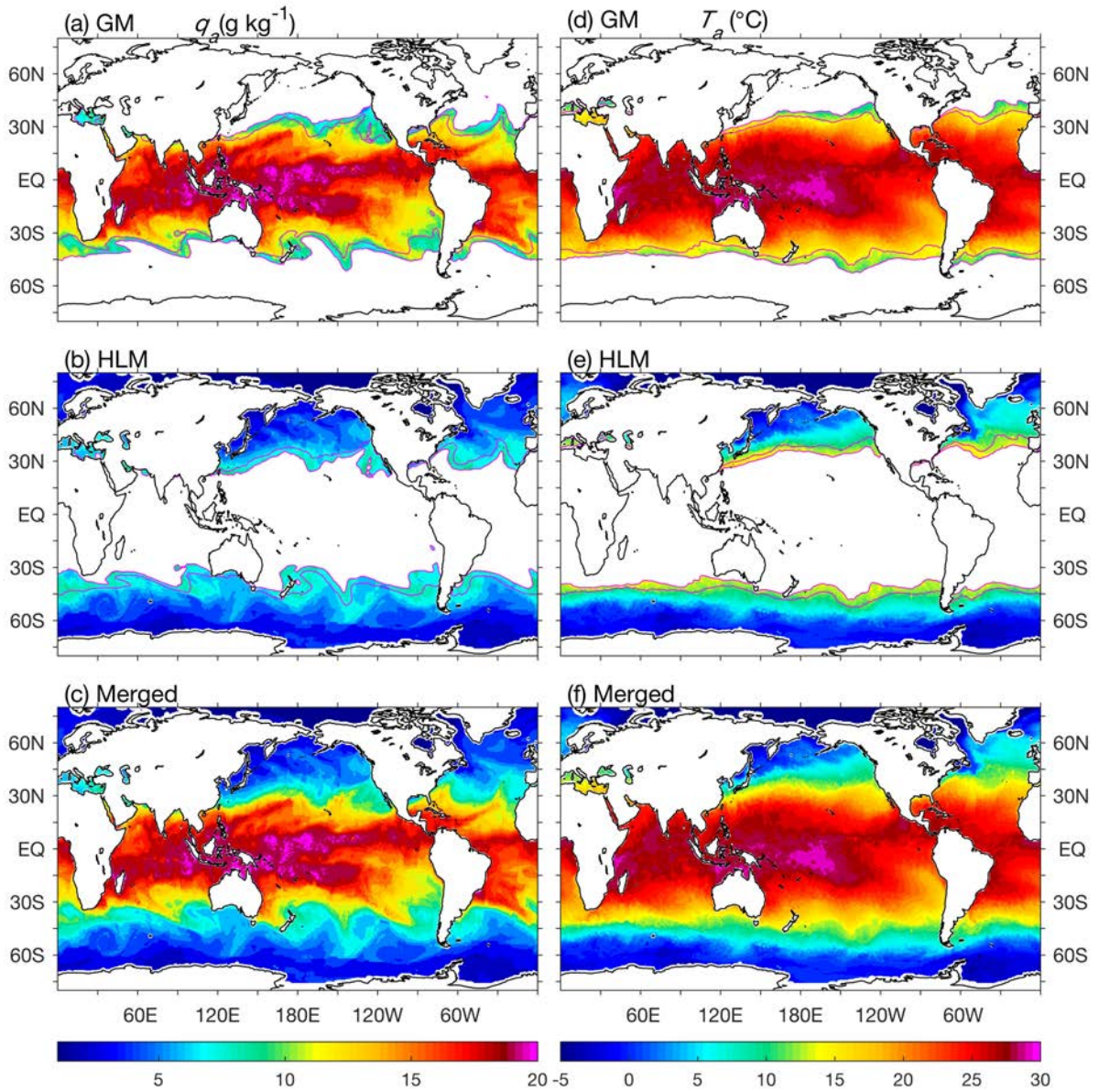
765



766

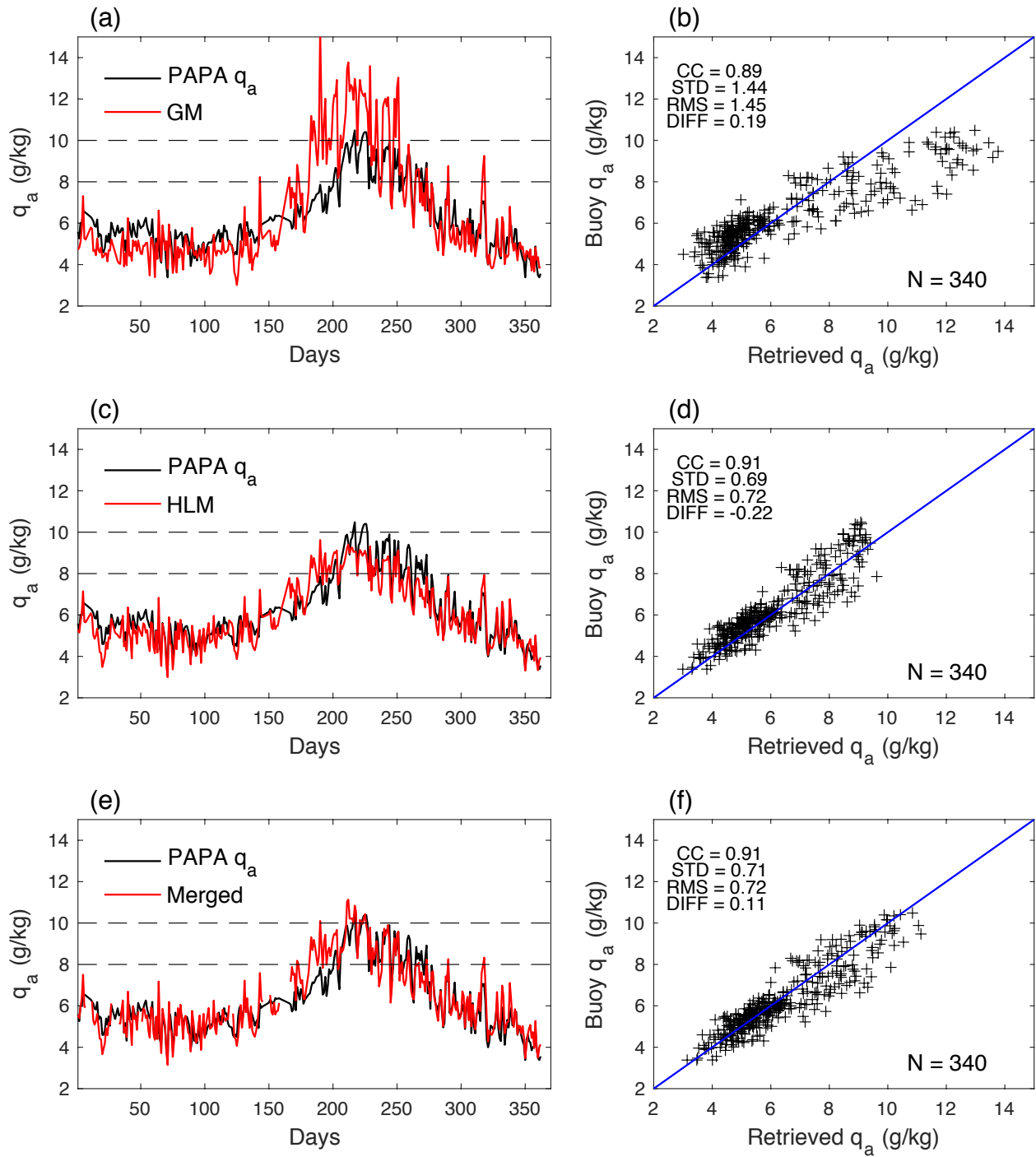
767 Figure 6

768



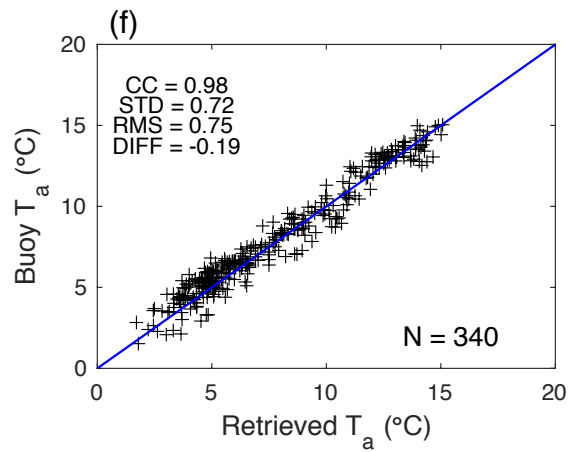
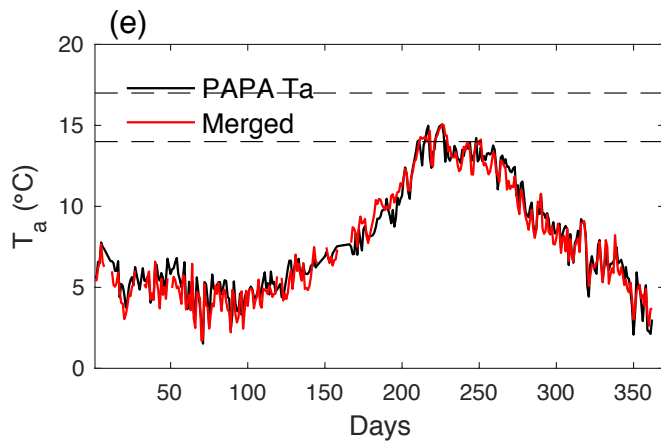
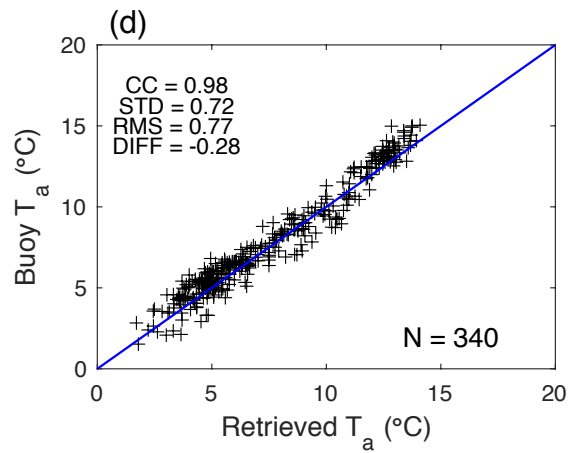
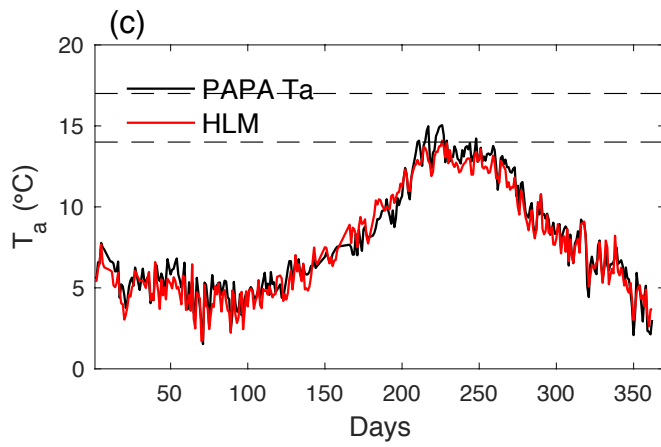
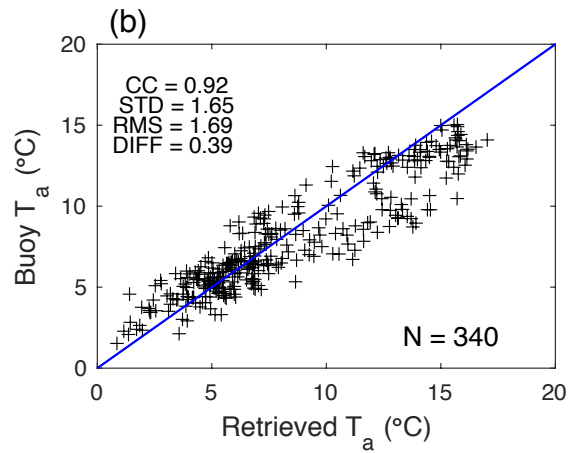
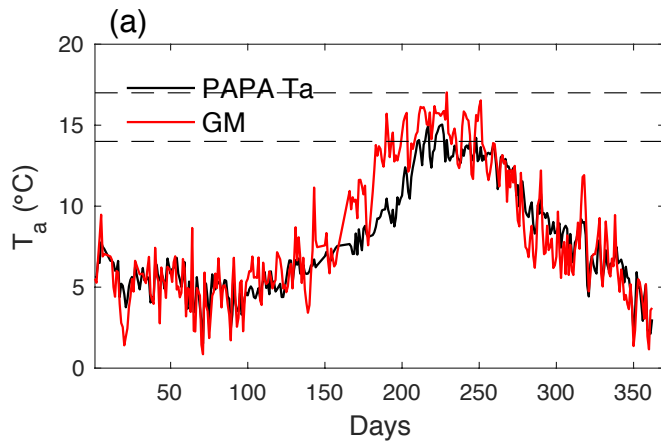
769

770 Figure 7



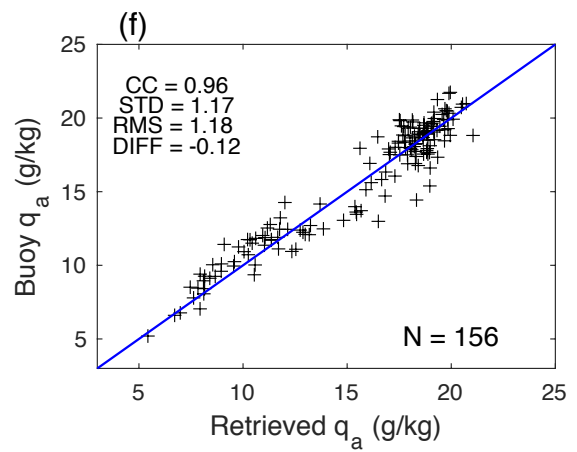
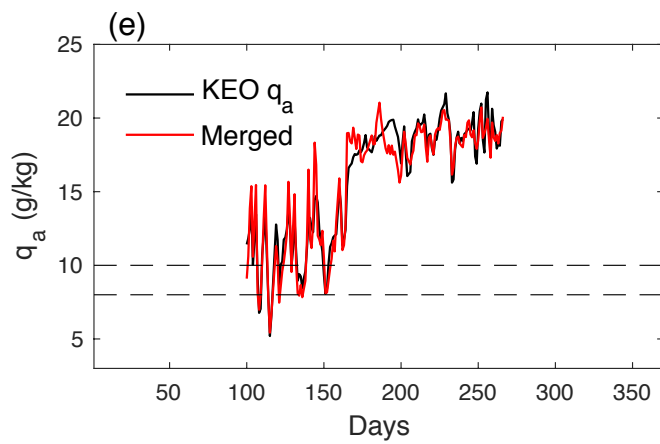
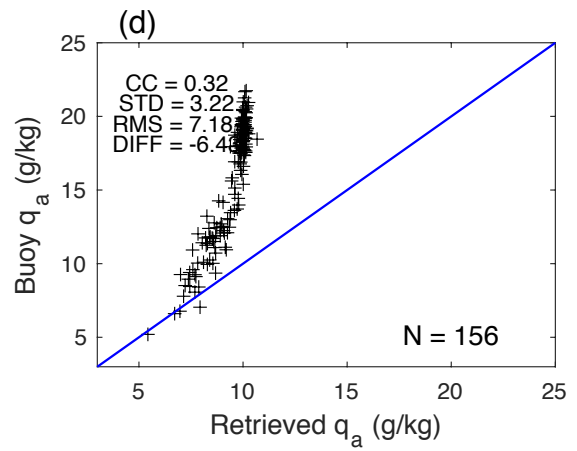
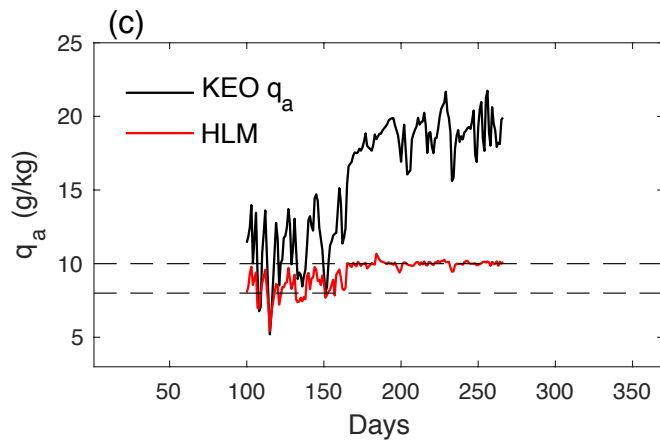
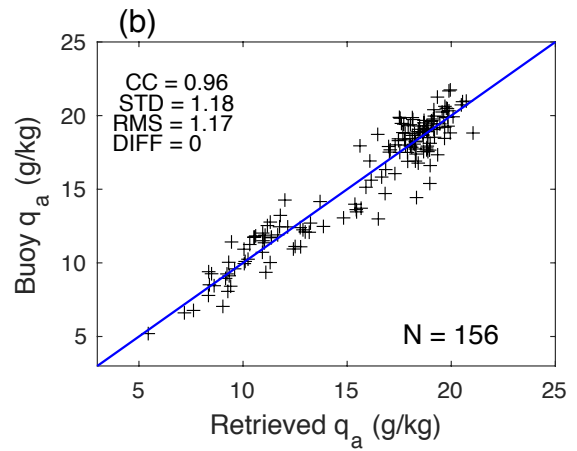
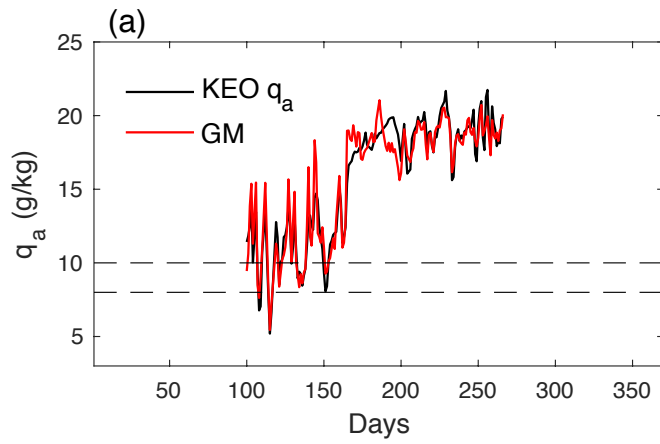
771

772 Figure 8



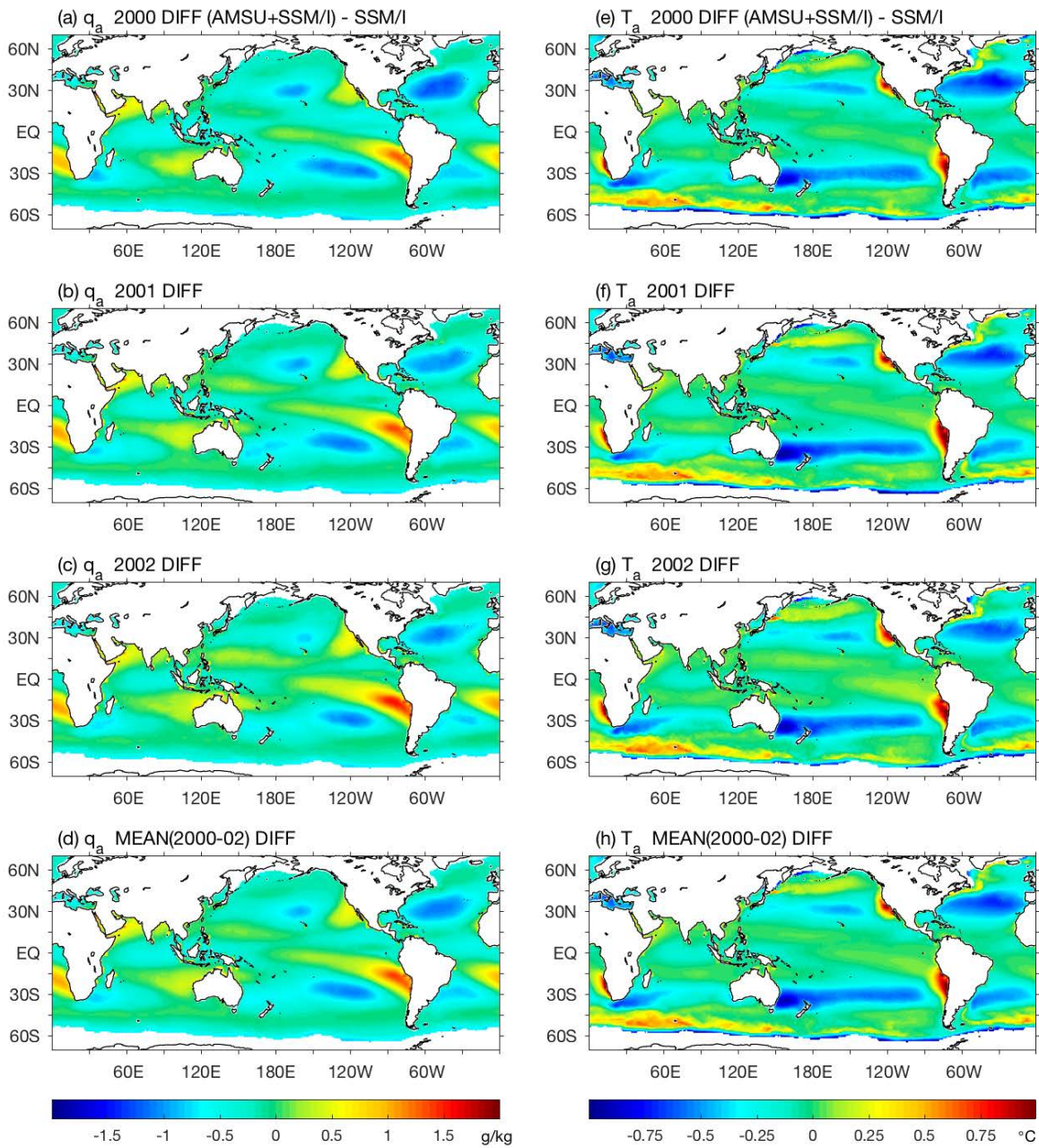
773

774 Figure 9



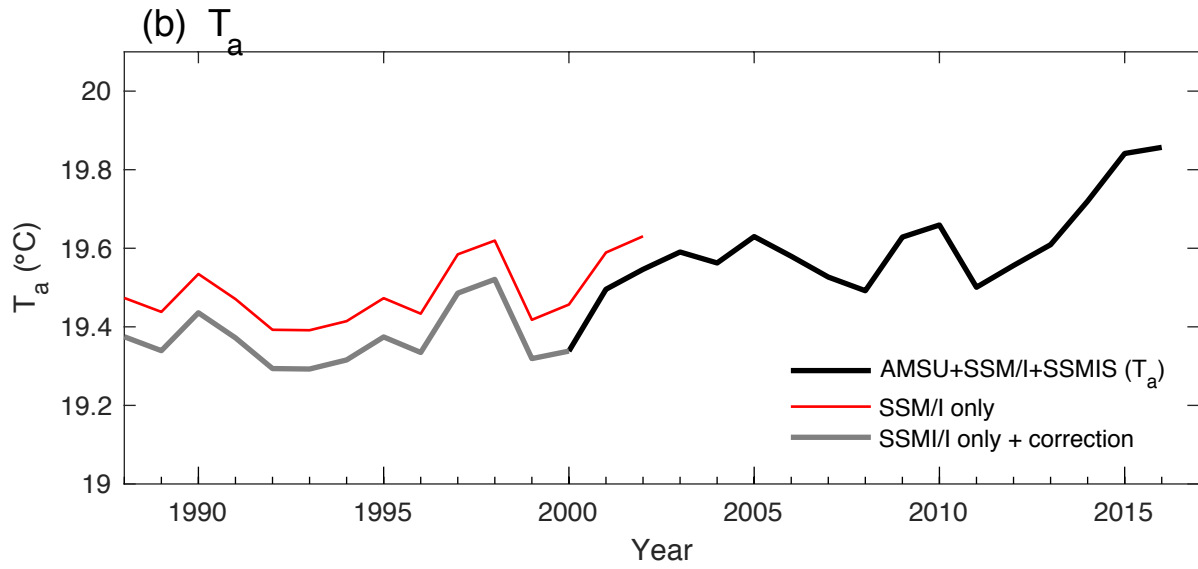
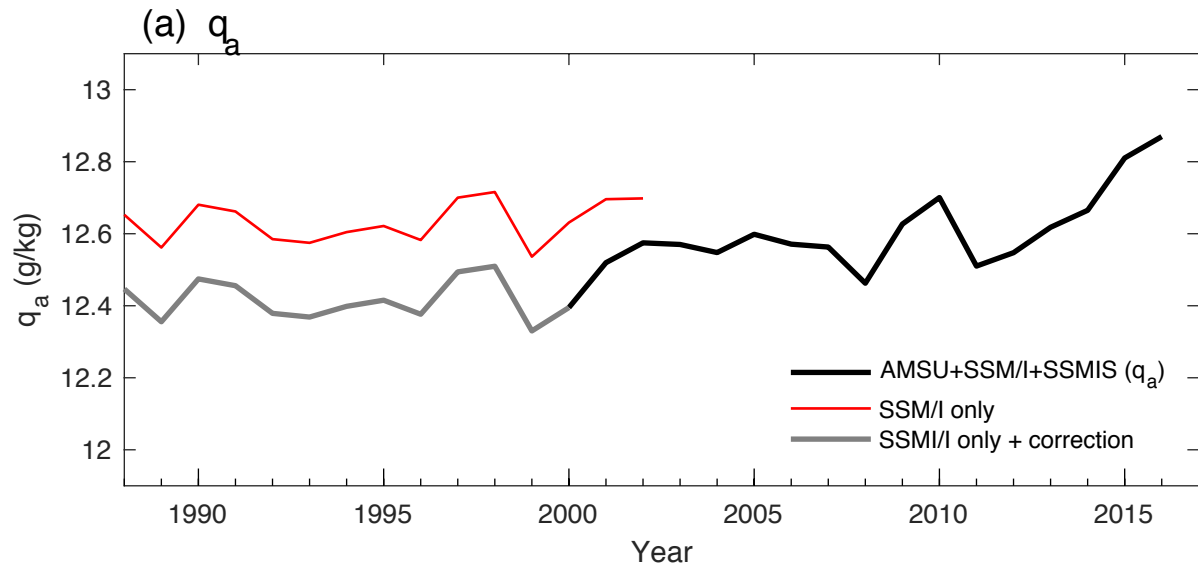
775

776 Figure 10



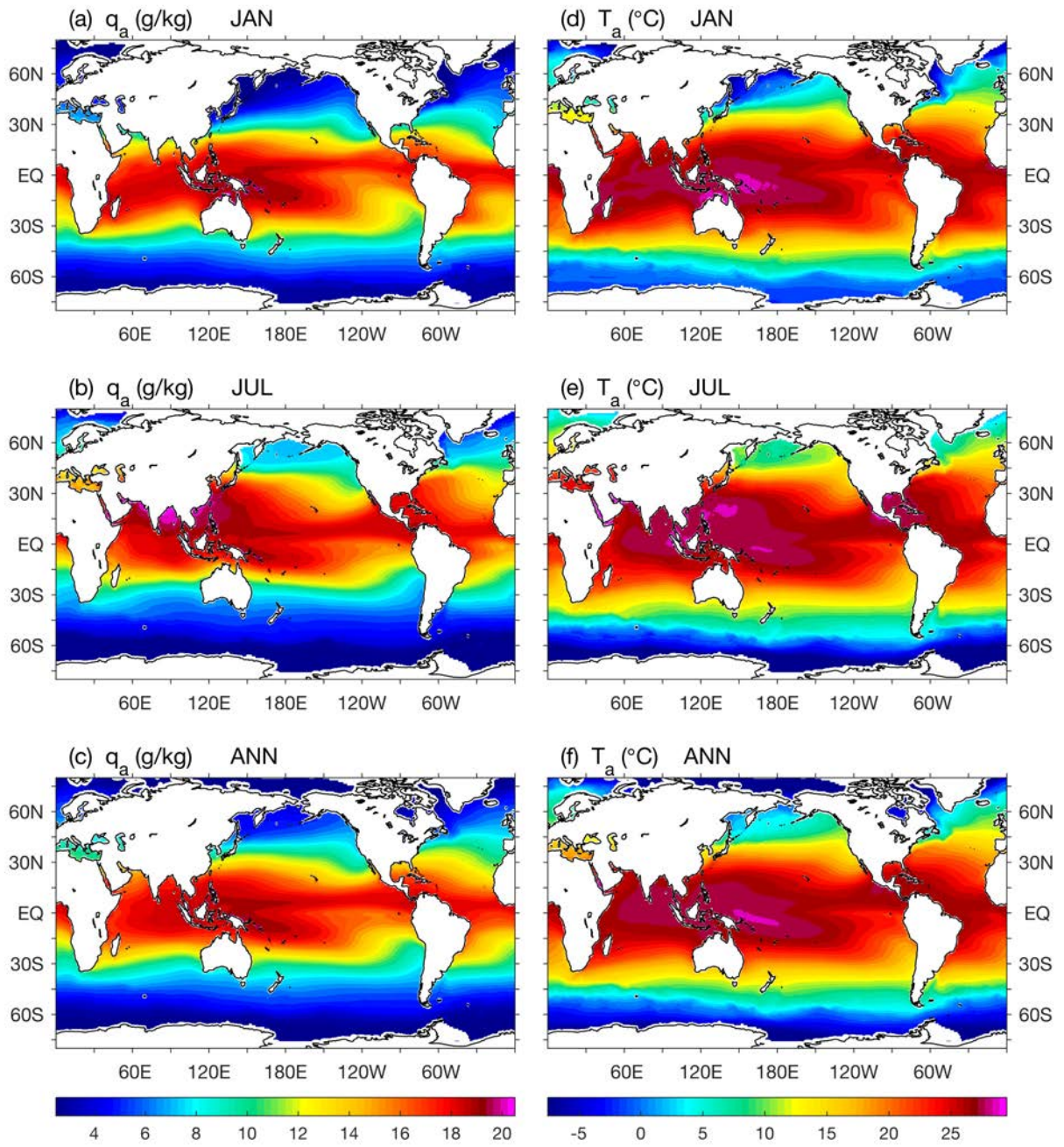
777

778 Figure 11



779

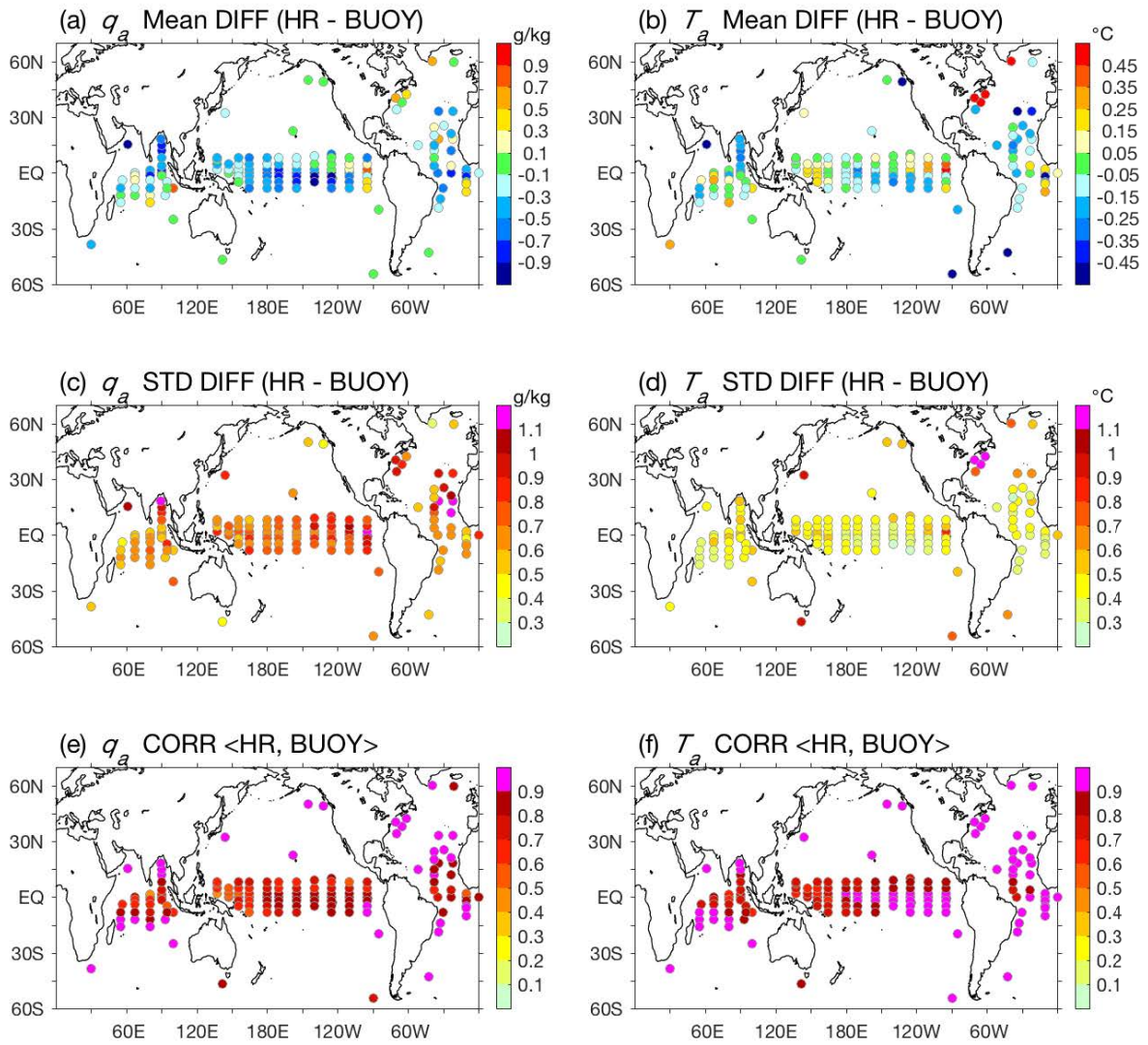
780 Figure 12



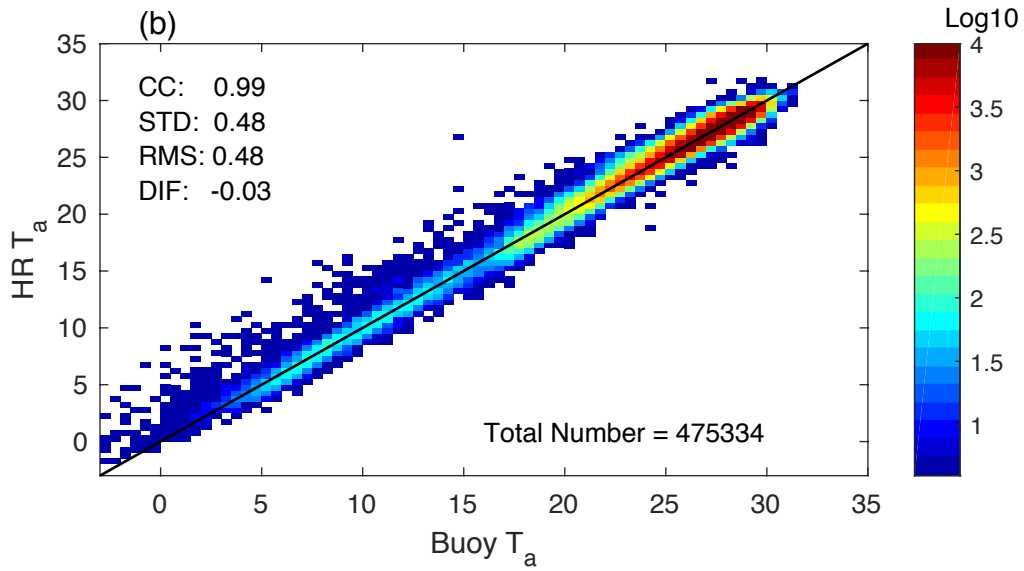
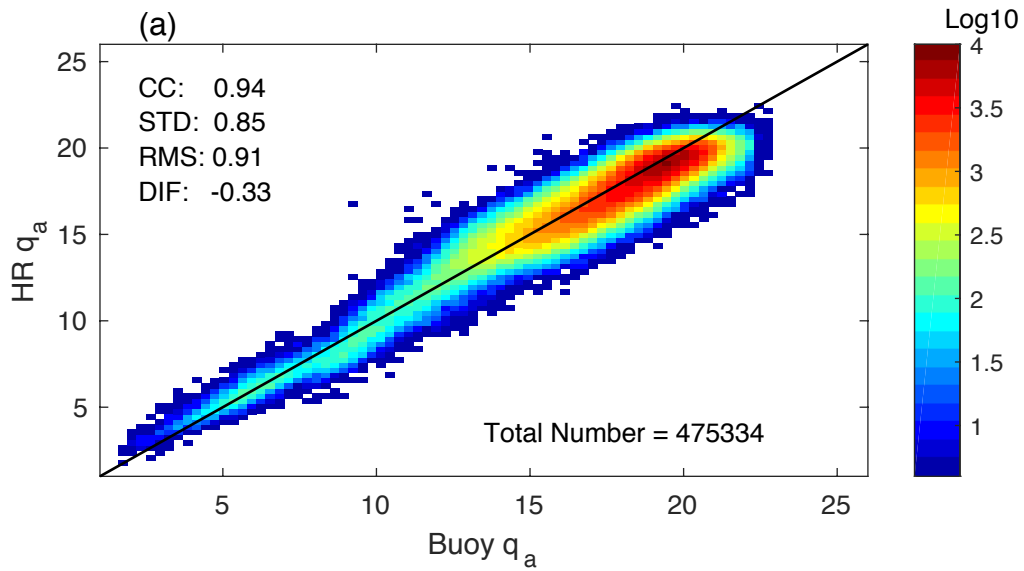
781

782 Figure 13

783 Figure 14



784  
785 Figure 14



786

787 Figure 15